Available online at www.sciencedirect.com

SCIENCE DIRECT

Sedimentary Geology 179 (2005) 249–278

Sedimentary Geology

www.elsevier.com/locate/sedgeo

Diagenesis of 1900-year-old siliceous sinter (opal-A to quartz) at Opal Mound, Roosevelt Hot Springs, Utah, U.S.A.

Bridget Y. Lynne *, Kathleen A. Campbell, J.N. Moore, P.R.L. Browne

University of Auckland, Geology Department, 23 Symonds Street, Aukland, New Zealand

Received 17 February 2005; received in revised form 25 May 2005; accepted 30 May 2005

Abstract

White, vitreous, siliceous sinter dated by ^{14}C at ~1900 years BP is located along the crest of the Opal Mound deposit at Roosevelt Hot Springs, Utah, U.S.A. Deposition at vents resulted from the Opal Mound fault opening conduits to the surface, allowing thermal fluids to discharge. Fault movement subsequently fractured the sinter and initiated a second period of fluid discharge. Colorful silica was deposited in this later period and formed the distal slope sinter, dated at ~1600 years BP. The sinter preserves both end-members in the mineralogical maturation of silica, from initial opal-A to mature quartz, and also records incremental intermediate steps, as revealed by X-ray powder diffractometry and by scanning electron, optical and Raman laser microscopy. Textural and mineralogical changes from one silica phase to another transpired gradually and gradationally. During diagenesis, incremental morphological changes alternated three times through nano- to micro-particle size transitions. The three corresponding mineralogical steps comprise: (1) opal-A to opal-CT, (2) opal-CT to opal-C, and (3) opal-C to quartz. Mineralogical changes preceded all morphological changes. Each step was initiated when silica nanostructures reached a critical diameter of 200 nm. The initial starting point of fresh (modern), polymeric, siliceous sinter deposition worldwide is nano-spherical particles of colloidal opal-A. Opaline sinter at Opal Mound is slightly more mature, reflecting the beginning of the aging process, and comprises botryoidal clusters of silica microspheres (<8 μm diameter). The conversion from these agglomerated microspheres to opal-CT bladed lepispheres at Opal Mound is marked by the reorganization of the microspheres into randomly oriented rows (~800 nm in length) of aligned nanospheres, up to 200 nm diameter. Each row merges into joined beads, which sharpen into classic opal-CT morphology of bladed lepispheres (~4 μm diameter). During this first diagenetic step, the X-ray powder diffraction trace undergoes an early shift in peak position, from ~4.0 to 4.09 Å, lining itself up in the position of the next more advanced mineralogical state, prior to emergence of the classic opal-CT blades. In the second step, the bladed lepispheres subsequently change into rectangular nano-rods (~50 × 100 nm long segments) during early opal-C development. During the third step of early quartz formation, the opal-C nano-rods recrystallize into groups of blocky nanostructures, each up to 200 × 300 nm. Quartz crystals grow at the expense of and pseudomorph opal-C, shown by remnant bands of blocky nanostructures at the base of the quartz crystals. Two generations of quartz crystals occur at Opal Mound: (1) diagenetic, which developed as opal-C nanostructures recrystallize to quartz; and (2) hydrothermal, formed by the injection of

* Corresponding author.

E-mail addresses: b.lynne@auckland.ac.nz (B.Y. Lynne), ka.campbell@auckland.ac.nz (K.A. Campbell), jmoore@egi.utah.edu (J.N. Moore), prl.browne@auckland.ac.nz (P.R.L. Browne).

0037-0738/$ - see front matter
doi:10.1016/j.sedgeo.2005.05.012

silica-infused thermal fluids into fractures and veins within the sinter deposit. Several silica phases commonly co-exist within individual samples. Moganite, a metastable silica phase, occurs with opal-CT, opal-C and diagenetic quartz, but is most abundant with opal-CT. Hence, the complete diagenetic continuum from opal-A to quartz is preserved within this sinter deposit. It formed in the short time span of ≤1900 years.

Keywords: Siliceous sinter; Diagenesis; Opal-A; Opal-CT; Opal-C; Moganite; Quartz; Silica phase; Morphology

1. Introduction

Siliceous hot spring deposits, or sinter, are common in geothermal regions where alkali chloride waters discharge at the surface after equilibrating with the underlying rocks at temperatures >175 °C (Fournier and Rowe, 1966). The silica is initially deposited as non-crystalline opal-A when the waters cool below 100 °C. The deposits entomb and silicify both biogenic and abiogenic material, and therefore provide valuable records of paleobiologic, paleohydrologic and paleoenvironmental conditions in these hydrothermal settings. However, recognition of depositional versus diagenetic components of sinters is a critical step if biogenic components are to be recognized through later physiochemical overprints (cf. Knoll and Walter, 1996). This problem is especially relevant for understanding the fossil record of early life on Earth, where geological events have often altered or destroyed biosignals (cf. Kerr, 2000). Later overprinting can be mistaken for depositional textures in these rocks, making it important to analyze younger deposits from analogous hydrothermal environments, so that the transformation of primary fabrics can be tracked as they undergo diagenesis (cf. Campbell et al., 2001; Guidry and Chafetz, 2003a; Lynne and Campbell, 2003, 2004). Because sinter diagenesis is patchy and inhomogeneous at all spatial and temporal scales, it is also necessary to reconstruct a detailed paragenetic history using an integrated micron-scale approach (cf. Farmer, 1999; Grotzinger and Knoll, 1999; Lynne and Campbell, 2004). This study evaluates fine-scale diagenetic changes that have occurred in vent, mid-slope and distal apron facies of the Opal Mound sinter deposit, Roosevelt Hot Springs, U.S.A., where the complete silica maturation sequence from opal-A to quartz has taken place within only 1900 years.

2. Silica mineral diagenesis

Morphological and mineralogical changes occur gradually and gradationally at the nano- to micro-scale, resulting in an intricate diagenetic process. This involves the progressive alteration of non-crystalline opal-A into paracrystalline opal-CT ± opal-C ± moganite, and eventually to microcrystalline quartz (Herdianita et al., 2000a). Such transitions can occur in deposits with little or no burial. Siliceous sinter initially deposits from solution as opal-A. We know of no study that has found other silica phases present. Recent work on modern and ancient sinter deposits suggests that complex dissolution, reprecipitation and recrystallization take place within pores during diagenesis to produce spatially patchy silica fabrics of differing mineralogical and morphological maturity (e.g., Cady and Farmer, 1996; Campbell et al., 2001; Guidry and Chafetz, 2003a; Lynne and Campbell, 2003, 2004). Lynne and Campbell (2003) reported two transitional phases between opal-A and opal-CT, evident in X-ray powder diffraction patterns, with maximum intensity peak positions of ~4.0 and 4.09 Å, respectively. Both transitional phases display a sharp-peaked scattering band centered at 4.09 Å, with the first designated as opal-A/CT (opal-A dominant) and the second as opal-CT/A (opal-CT dominant). Lynne and Campbell (2004) reported that these diagenetic mineralogical changes precede microstructural morphological changes from opal-A to opal-CT. Herdianita et al. (2000a) demonstrated that the phase transitions from opal-A microspheres, to opal-CT ± opal-C bladed lepispheres, and eventually to blocky, microcrystalline quartz, are accompanied by an increase in density and decrease in porosity. Hence, a maturation model was developed for undisturbed New Zealand sinters, with an age estimate for transformation to quartz of ~ 40,000 years (Herdianita

et al., 2000a). However, Rodgers et al. (2004) noted that diagenetic states within or between individual outcrops vary considerably, so that the model can only be applied in the most general terms. Hence, mineralogical maturation cannot be used as a guide to the age of a sinter deposit, as diagenesis proceeds at different rates within each deposit. The presence of organic matter or other minerals (e.g., carbonates) may inhibit or accelerate the maturation rate (Herdianita et al., 2000a, Fig. 8, p. 59). Moreover, sinter weathering or overprinting by acidic steam condensate can also affect rates of diagenesis (Lynne and Campbell, 2004).

Siliceous marine sediments, wood petrification, and silica residue undergo the same progressive mineralogical transformations as outlined above. Lynne and Campbell (2004, and references therein), summarized previous research and outlined several mechanisms that affect siliceous sinter formation. These include pH changes, variations in fluid chemistry, seasonality, hydrodynamics and evaporation/cooling ± wicking. However, the physicochemical factors controlling silica mineral diagenesis at the nanometer scale still remain uncertain, and await experimental or theoretical assessment outside the scope of this study.

3. Previous studies and the geologic setting of Roosevelt hot springs

Roosevelt Hot Springs is among the largest and hottest of the more than a dozen geothermal resources in the Basin and Range Province, U.S.A. It is a north-trending horst, located near the eastern margin of the province, on the western flank of the Mineral Mountains (Fig. 1), and bounded by Basin and Range normal faults. The geothermal reservoir, which covers an area of approximately 32 km^2, is developed in fractured Precambrian gneiss and Tertiary granite (Christensen et al., 1983; Ward et al., 1978; Moore and Nielson, 1994). Fluid circulation is controlled by high-angle normal faults trending northerly and easterly, and westward dipping, low-angle normal faults (Neilson et al., 1978; Sibbett and Nielson, 1980). Hydrothermal-alteration mineral assemblages of the reservoir host rocks were reported by Parry et al. (1979) and Moore and Nielson (1994). Wells drilled to depths of 1770 m encountered temperatures as hot as 268 °C (Capuano and Cole, 1982). The deep reservoir fluids are alkali chloride in character with a near-neutral pH. Fluids discharged from three of the wells are used at the Blundell power plant, commissioned in 1984, which generates 26 MW (gross) of electrical power (Blackett and Ross, 1992). The geothermal system is believed to be driven by heat from a young intrusion related to rhyolite domes emplaced beneath the crest of the Mineral Range. The pluton is 250 km^2, the largest and youngest in Utah, with K–Ar dates from 9.4 to 14 Myr (Armstrong, 1970; Park, 1971; Ward et al., 1978; Parry et al., 1979).

Sinter deposits at Roosevelt Hot Springs occur primarily along the Opal Mound fault (Fig. 1), a north-trending structure defining the western boundary of the geothermal system. The largest sinter deposit at Opal Mound is located in the southern end of the field. Moore and Nielson (1994) recognized two generations of sinter deposition, the younger consisting of brightly colored sinter, and the older of white, vitreous sinter. They postulated that the hot spring system had undergone at least two stages of activity, with the Opal Mound fault serving as the fluid conduit for both. No historical activity at the Opal Mound deposit has been reported, although wells drilled adjacent to the deposit encountered hot water at a depth of 365 m. Bamford et al. (1980) found other volumetrically minor hot spring deposits cemented by calcite, manganese-oxide and hematite, which also occur elsewhere along the Opal Mound fault trace. These were not analyzed in this study. The concentrations of trace elements in the fluids are spatially disjunct, and reflect physical and chemical changes including conductive cooling, and boiling and mixing with calcium-rich groundwaters (Christensen et al., 1983; Moore and Nielson, 1994). Outside the study area, but adjacent to the northern part of the field, present-day thermal activity is limited to fumaroles, which reflects a lowering of the piezometric surface.

4. Sample characteristics

Twenty-five sinter samples from Opal Mound were collected for study and represent vent, proximal vent,

middle and distal-apron slope facies (Fig. 1B). These were further subdivided into 48 sub-samples that target individual horizons that have visible color or textural changes. The Munsell color chart (1992) was used to standardize the range in sample colors (Table 1). Samples from the Opal Mound vent area

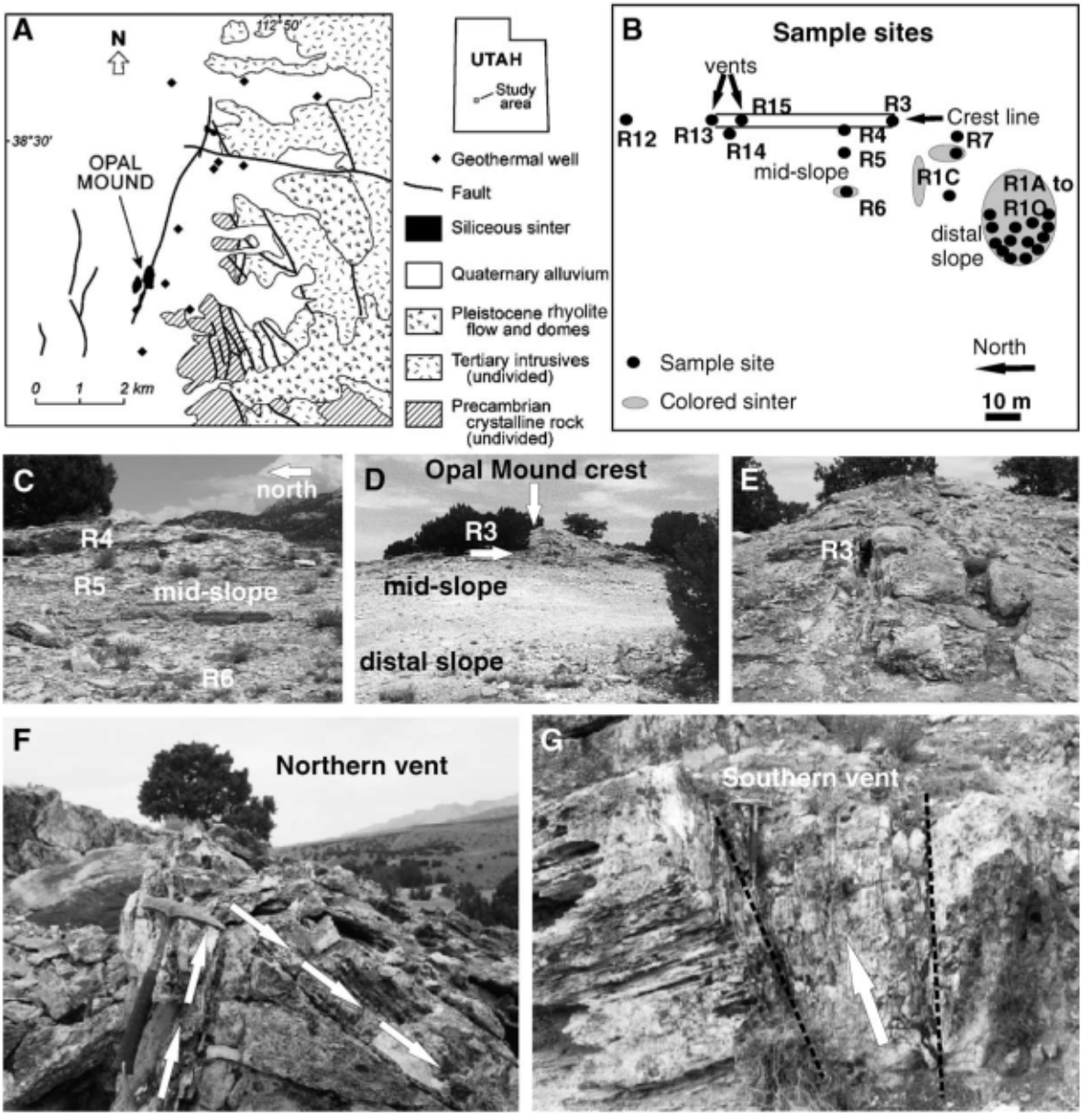

Fig. 1. Location map and sample sites. (A) Map showing the location of Opal Mound and the surrounding geology. (B–E) Field sample sites, which are shown by the letter R, followed by a number. (B) Locations of sample sites and white versus colored sinter. (C) Mid-slope sinter apron with location of sample sites R4–R6. (D) Overview of the Opal Mound looking north, showing vent and proximal-vent deposits, and mid- and distal-slope deposits. Location of sample site R3. (E) Southern end of Opal Mound, with sample site R3. (F) Silicified northern vent, site R13; arrows show direction of outflow. (G) Silicified southern vent, site R15; arrow shows direction of upward flow from vent.

Table 1
Sinter sample colors compared with Munsell chart color, value, chroma and hue standardizations

Sample color	Color	Value	Chroma	Hue
Yellow	Yellow	8	8	2.5Y
Orange	Yellowish red	6	8	5YR
Tan	Yellowish red	6	4	5YR
Brown	Dark brown	4	3	7.5YR
Red	Dusky red	3	3	5R
Pink	Weak red	5	3	5R
Cream	Pale yellow	8	2	2.5Y
White	White	8	1	7.5YR
Clear	Light grey	7	1	2.5Y

consist of white, vitreous sinter. Mid-slope samples are faintly colored and comprise vitreous or porous indurated sinter; whereas, distal-slope samples are dominantly composed of vibrantly colored, vitreous or porous indurated sinter. Sample descriptions are presented in Table 2. Along the crest of the Opal Mound deposit, erosion has exposed two discharge vents, here referred to as the northern and southern vents (Fig. 1F, G).

5. Methods

Mineralogical and morphological transitions were traced by X-ray powder diffraction (XRPD), scanning electron microscopy (SEM), density and porosity measurements, use of a Friability Index (FI), retardation values, optical and Raman microscopy, and by trace element analysis. Furthermore, two radiocarbon dates were obtained for the deposit.

X-ray powder diffraction (XRPD) is the principal technique used to determine the silica phase mineralogy, as well as to compare the degree of lattice order/disorder among samples. The diffractometer used and its operating conditions are described in detail in Lynne and Campbell (2004). In brief, dry, untreated samples were scanned at 0.6° 2θ/min, with a step size of 0.01°, from 10–40° 2θ. Operating conditions were 40 kV and 20 mA, using CuKα radiation ($\lambda\alpha 1 = 1.54051$ Å). Interpretation of sinter XRPD traces follows the methodology outlined in Herdianita et al. (2000b). The raw XRPD traces were not electronically manipulated. A curve and base line were fitted manually, from which the full width at half maximum intensity (FWHM) was measured.

The FWHM of the distinctive ~4 Å diffraction band is a guide to the degree of lattice ordering within each silica phase (Herdianita et al., 2000b). Lattice ordering increases with mineralogical maturation, from opal-A to opal-A/CT to opal-CT to opal-C and ultimately to quartz. The lower the FWHM value, the sharper the peak, the more ordered the silica structure and, hence, the more mineralogically mature the sinter. Silica nomenclature is that of Smith (1997, 1998). Non-crystalline opal-A, opal-A/CT, and para-crystalline opal-CT silica phase mineralogies produce XRPD patterns characteristic of wide bands, or broadbands. Para-crystalline opal-C and micro-crystalline quartz however, produces XRPD traces with sharp peaks. Prominent diffraction bands for opal-A are centered at ~4Å (~22.2° 2θ), for opal-CT at 4.09Å (21.75° 2θ), and for quartz peaks at 4.257Å (20.85° 2θ; Jones and Segnit, 1971; Flörke et al., 1991; Smith, 1998).

In this study, detailed analysis of samples revealed a wide range of broadbands and maximum intensities. This variation in X-ray characteristics of the samples reflects changes in silica ordering from non-crystalline opal-A, which lacks any long-range order, to the mixed cristobalitic and tridymitic stacking sequences of para-crystalline opal-CT, and finally to the ordered structure of microcrystalline quartz (e.g., Flörke et al., 1991; Graetsch, 1994; Smith, 1998).

The Renishaw Raman 1000 laser microprobe, in contrast to XRPD analysis, allows targeting of specific grains and is used primarily in sinter studies to distinguish between moganite and quartz (cf. Rodgers and Cressey, 2001; Rodgers and Hampton, 2003). The most intense XRPD reflection of moganite occurs at 26.726° 2θ and this overlaps with the main quartz reflection at 26.68° 2θ. The second most intense moganite reflection occurs at 26.303° 2θ. However, due to its low intensity relative to the quartz in the Opal Mound samples and low signal to noise ratio, it is difficult to recognize the presence of moganite by using only XRPD. Moganite is a metastable silica phase that can form prior to quartz. Previous studies identifying silica phases with the Raman microprobe have shown that the principal microcrystalline quartz peak occurs at 465 cm^{-1}, whereas the principal moganite peak is at 501 cm^{-1} (Kingma and Hemley, 1994; Götze et al., 1998; Rodgers and Cressey, 2001; Rodgers and Hampton, 2003). Para-crystalline opal-C produces a peak at 777 cm^{-1}. Where both para-crys-

Table 2
Opal Mound siliceous sinter sample descriptions (N=north, S=south, W=west)

AU number	Field number	Location	Sample description
55338–55342	R1A	Distal sinter apron, SW slope of Opal Mound crest	Alternating yellow, orange, and tan; porous indurated, undulose horizons < 5 mm thick with sharp boundary contacts. 4 horizons (AU55339–AU55342) and bulk sample (AU55338).
55354	R1E	Distal sinter apron, SW slope of Opal Mound crest	Finely laminated red, pink, white, and yellow vitreous silica; with sharp planar boundary contacts. Uppermost layer grades into thicker bands, (<3 mm) of pink, tan, and yellow vitreous sinter.
55361	R1G	Distal sinter apron, SW slope of Opal Mound crest	Alternating horizons of 2 mm thick, red, pink, white, and tan vitreous silica with sharp planar boundary contacts.
55355–55360	R1F	Distal sinter apron, SW slope of Opal Mound crest	3 horizons of porous indurated sinter colored pink, white, and yellow, and 2 horizons of vitreous silica with planar boundary contacts (AU55356–AU55360). Bulk sample, AU55355.
55362–55365	R1I	Distal sinter apron, SW slope of Opal Mound crest	Pink, red, and white, vitreous silica with sharp planar boundary contacts (AU55363–AU55365). Bulk sample, AU55362.
55343–55346	R1B	Distal sinter apron, SW slope of Opal Mound crest	Red (AU55346) tan (AU55344) and clear (AU55346) vitreous silica horizons forming sharp, undulose boundary contacts. AU55343, bulk sample.
55366	R1K	Distal sinter apron, SW slope of Opal Mound crest	Porous indurated sinter with alternating, undulose horizons of tan, yellow, and pinks.
55367	R1L	Distal sinter apron, SW slope of Opal Mound crest	Lowermost horizon comprises clear vitreous silica grading into yellow, and then red vitreous sinter. All contacts are gradational and undulose.
55371	R1O	Distal sinter apron, SW slope of Opal Mound crest	Alternating horizons of pink, yellow, and tan vitreous silica with a thin veneer of white silica that is brecciated and overlies the colored sinter.
55350–55353	R1D	Distal sinter apron, SW slope of Opal Mound crest	3 horizons (AU55351–AU55353) and bulk sample (AU55350).
55368–55370	R1M	Distal sinter apron, SW slope of Opal Mound crest	Clear (AU55369) and tan (AU55370) vitreous silica with sharp upper boundary contacts. Bulk sample, AU55368.
55347–55349	R1C	Mid-sinter slope	Clear, vitreous silica horizon, gently undulose with sharp boundary contact (AU55349). White, vitreous silica (AU55348). Sharp but gently undulose boundary contacts. Bulk sample AU55347.
55377–55379	R6A	Mid-sinter slope	Thinly laminated alternating horizons of brown, cream, and white vitreous silica. Bulk sample (AU55377), white vitreous layer (AU55379), and clear layer (AU55378).
55380	R6B	Mid-sinter slope	Alternating horizons of pink, red, and clear vitreous silica directly beneath R6A. AU55380.
55381–55382	R6B2	Mid-sinter slope	Alternating horizons of pink and red (AU55381), and clear (AU55381) vitreous silica directly beneath R6B.
55383–55385	R7	Opal Mound crest	White vitreous sinter (AU55384) with rare porous sinter (AU55385). Bulk sample, AU55383.
55386	R8	Mid-sinter slope	Alternating horizons of clear, red, pink, and yellow vitreous silica. Some horizons are <1 mm thick; others are up to 5 mm thick.

Table 2 (*continued*)

AU number	Field number	Location	Sample description
55395	R15	Southern vent on Opal Mound crest	Tan colored, porous indurated sinter.
55387	R12	30 m N of northern vent, in alignment with Opal Mound crest	White, vitreous silica with porous indurated, cream colored silica patches.
55392–55393	R14	W side of northern vent along Opal Mound crest	R14A: White vitreous silica (AU33393). R14B: Thinly laminated, cream, porous indurated and friable silica (AU55392).
55372	R3	Southernmost exposure of sinter along Opal Mound crest	White vitreous silica.
55373	R4	15 m N of R3	White vitreous silica.
55374–55376	R5	15 m N of R3	Multiple, <10 mm thick, white vitreous silica horizons with 1 mm wide voids between most horizons; AU55375, AU55376. Bulk sample, AU55374.
55388–55391	R13	Northern vent on Opal Mound crest	4 laminae of white vitreous silica (AU55389–AU55392). Bulk sample, AU55388.

talline tridymite and cristobalite are present in the silica lattice as opal-CT, the bands merge to form a single peak at 422 cm^{-1}. Non-crystalline opal-A produces a flat line with no peak.

A Renishaw Raman 1000 laser microprobe system with deep depletion CCD was used to analyze 21 spots within eight samples following the methods outlined in Rodgers and Hampton (2003). Data were collected through the range of 200 to 1000 cm^{-1} with a solid state diode red laser set at 785 nm and 25 mW. Using a 1200 l/min diffraction grating and cosmic ray inhibitor, spectra were collected with a slit of 100 μm and an integration time of 10 s under 100% power. Five consecutive spectral runs for each sample were collected and combined to improve the signal-to-noise ratio. The Raman was calibrated with calcite (1085 cm^{-1} peak) and silicon (520 cm^{-1} peak). Scanning electron microscopy (SEM) and electron diffraction spectroscopy (EDS) were performed on selected sinter samples coated with platinum, following methods described by Lynne and Campbell (2004). The thickness of each thin section was measured and the retardation value calculated from the Michel–Levy chart. Density and porosity calculations were obtained by methods outlined in Battey and Pring (1977). The Friability Index (FI) was used to compare the cohesive strength of the sinter samples as described in Lynne and Campbell (2004).

X-ray Fluorescence (XRF) analyses were made of 11 bulk samples selected to cover a range of mineralogical states; two vent, one proximal vent, four mid-slope, and four distal apron deposits. Each was crushed in a tungsten carbide grinder to produce 10 g of powder, which was mixed thoroughly with 1 ml of polyvinylpyrrolidine (PVP) and methyl cellulose in water and ethanol. Samples were mechanically pressed to >15 tonnes/kg into 40 mm wide circular moulds. Once removed from the mould, samples were oven dried overnight. A Siemens SRS 3000 sequential X-ray spectrometer with a Rh tube was used to make a semi-quantitative analyses, and the results calibrated for all elements using three multi-element glass beads and a graphite disk. Brucker Spectra-plus (ver. 1.51) software was used to reduce the data. Precision was checked by running four samples twice, with each run producing very similar results.

Laser Ablation Inductively Coupled Plasma Mass Spectrometry (LA-ICPMS) was performed at the Australian National University, Canberra, on seven locations within two samples to determine trace element content for specific textures. Procedures and operating conditions are detailed by Eggins et al. (1997) and Ridley and Lichte (1998).

One sample of white, vitreous siliceous sinter from the vent area, and one of colored, distal-apron sinter, were dated by accelerator mass spectrometry (AMS) at the Rafter Radiocarbon Laboratory, Institute of Geological and Nuclear Sciences Ltd, Lower Hutt, New Zealand. Pollen and plant fragments were extracted for calibrated ^{14}C-dating following methods outlined in Lynne et al. (2003).

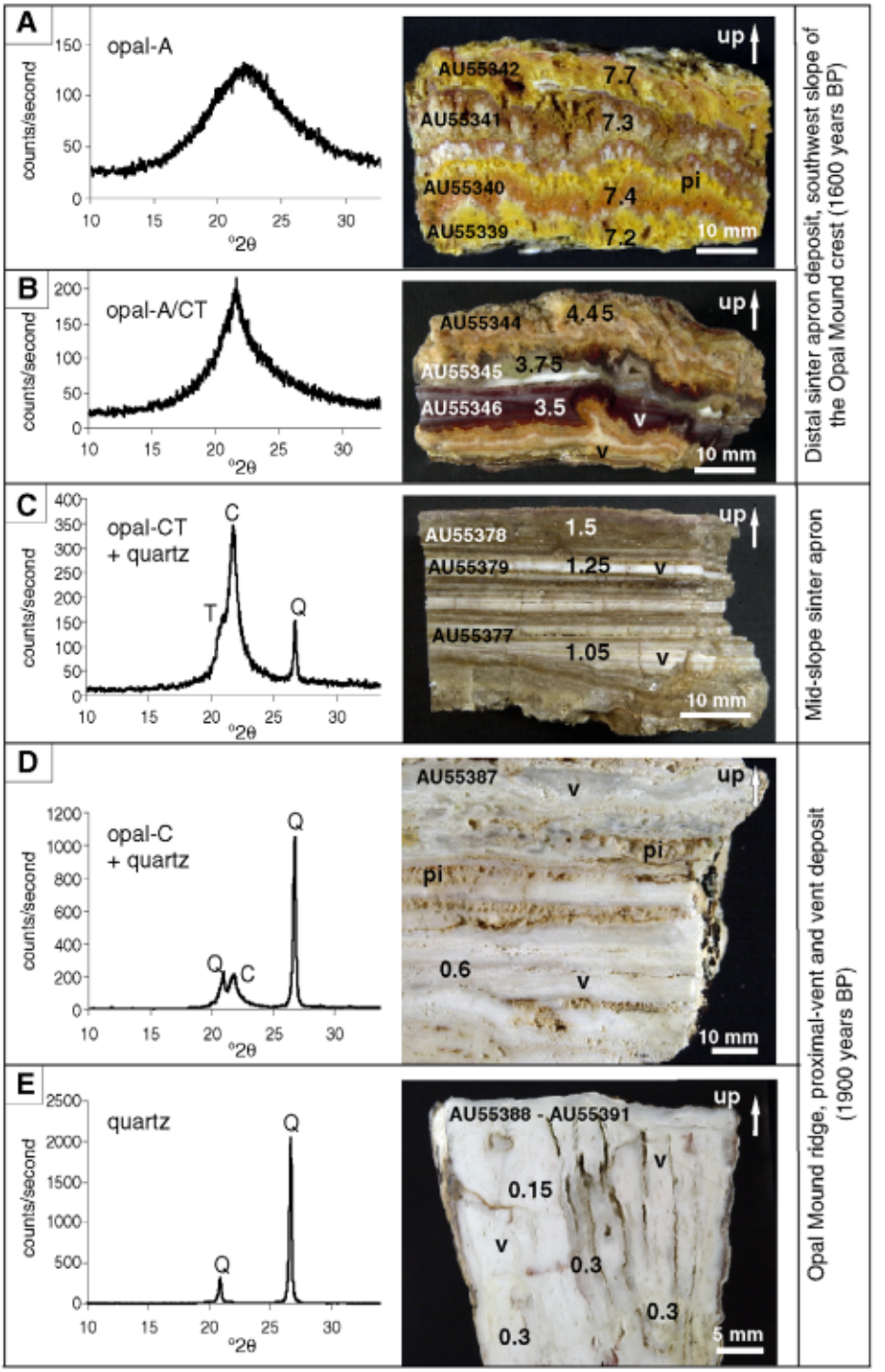
A
opal-A
counts/second
°2θ
AU55342
7.7
AU55341
7.3
AU55340
7.4
pi
AU55339
7.2
up
10 mm
B
opal-A/CT
AU55344
4.45
AU55345
3.75
AU55346
3.5
v
v
C
opal-CT
+ quartz
C
T
Q
AU55378
1.5
AU55379
1.25
AU55377
1.05
D
opal-C
+ quartz
Q
C
AU55387
pi
0.6
E
quartz
AU55388 - AU55391
0.15
0.3
0.3
0.3
5 mm
Distal sinter apron deposit, southwest slope of the Opal Mound crest (1600 years BP)
Mid-slope sinter apron
Opal Mound ridge, proximal-vent and vent deposit (1900 years BP)

6. Results

The sinter at Opal Mound preserves the entire silica phase mineralogical continuum from opal-A through to quartz (Figs. 2 and 3). Results are divided into six sections: AMS dating, mineralogy, physical sinter characteristics, trace element analysis, microbial textures, and morphological changes accompanying silica mineral phase transitions.

6.1. Age of the opal mound sinter

Two AMS radiocarbon dates were determined for the Opal Mound sinter. Topographically higher, white, vitreous silica from the vent area is 1920 ± 160 years old; whereas the colored sinter deposits on the mid-to lower slopes is 1630 ± 90 years old.

6.2. Mineralogy

47 sub-samples were analyzed by XRPD to determine their silica phases. Samples were selected across the entire spatial extent of the deposit, from vent to distal-sinter apron, to identify any trends or inconsistencies within the Opal Mound sinter. Results are shown in Table 3. A progressive decrease in silica phase maturation values occurs with distance away from Opal Mound ridge. The northern vent (Fig. 1F) and near-vent deposits comprise mineralogically mature quartz and are older; whereas the distal slope, colored sinter consists of immature opal-A and is younger. Transformation to quartz within this deposit occurs rapidly as compared to quartz sinters of New Zealand which can take at least an order of magnitude longer to reach the same mineralogical state (Herdianita et al., 2000a). The FWHM values of these two mineralogical end members are 7.70° 2θ (1.36 Å), and 0.15° 2θ (0.03 Å), respectively. Systematic and progressive morphologic transitions track the change from opal-A to quartz (Fig. 3). For each stage of the transformation, mineralogical changes preceded morphological modifications (cf. Lynne and Campbell, 2004), where the impending silica phase transition can be identified initially by a slight shift to a larger d-spacing and sharpening of the peak reflection. The XRPD results are divided into five groups (Table 3), based on their silica phase maturation state as determined by the shape of the XRPD band and the corresponding FWHM value (cf. Lynne and Campbell, 2003, 2004). A range of FWHM values occur within each group. Typical XRPD patterns for each group are shown in Fig. 2. XRPD results of bulk and sub-samples indicate that variability in silica phase occurs not only over lateral distances at the microscale, but it also occurs over stratigraphic distances of only millimeters. For example, sample AU55377 (Fig. 2C) contains: (1) a bulk sample (AU55377), FWHM = 1.05° 2θ; (2) a sub-sample (AU55379), of white vitreous horizon, FWHM = 1.25° 2θ; and (3) a sub-sample (AU55378), of a clear vitreous horizon, FWHM = 1.5° 2θ. Thus, mineralogical changes are progressive and gradational within specific layers. Therefore, caution must be exercised when analyzing bulk samples because subtle but significant mineralogical changes may be overlooked.

The Raman laser microprobe was used to detect moganite in samples across the entire diagenetic continuum from opal-A to quartz, where XRPD determined FWHM values ranging from 6.7° to 0.2° 2θ (Table 4). Moganite was not detected in samples containing opal-A or opal-A/CT silica phases. However, samples with opal-CT + quartz, opal-C + quartz, or quartz all displayed moganite peaks of varying maximum intensities. The strongest moganite peak was obtained in sample AU55379, which consists of opal-CT + quartz and has a FWHM value of 1.25° 2θ.

Fig. 2. Incremental mineralogical steps in the transformation of opal-A to quartz at Opal Mound, illustrated with typical XRPD traces and hand specimen photographs. AU numbers = sub-sample numbers. Numerical values = full width at half maximum intensity (FWHM, in °2θ) determined for various horizons; v = vitreous, pi = porous indurated. (A) Opal-A. Microbial-rich sinter with alternating, undulating horizons of yellow, orange, tan, and white. Sub-sample trace from AU55342. (B) Opal-A/CT. Three different colored vitreous horizons: tan, clear, and red, containing preserved microbes. Sub-sample trace from AU55344. (C) Opal-CT. Multiple brown, and white, horizontal, vitreous laminae with sharp contacts. Sub-sample trace from AU55379. (D) Opal-C + quartz. White, vitreous silica with minor patches of cream-colored, porous indurated silica. Sub-sample trace from AU55387. (E) Quartz. Multiple, vertical laminae of white, vitreous silica <10 mm thick, capped by a single 10 mm thick horizon of white vitreous silica. Northern vent sample; the vertical bands were deposited by fluid ascending from the bottom to top of the sample. Sub-sample trace from AU55389.

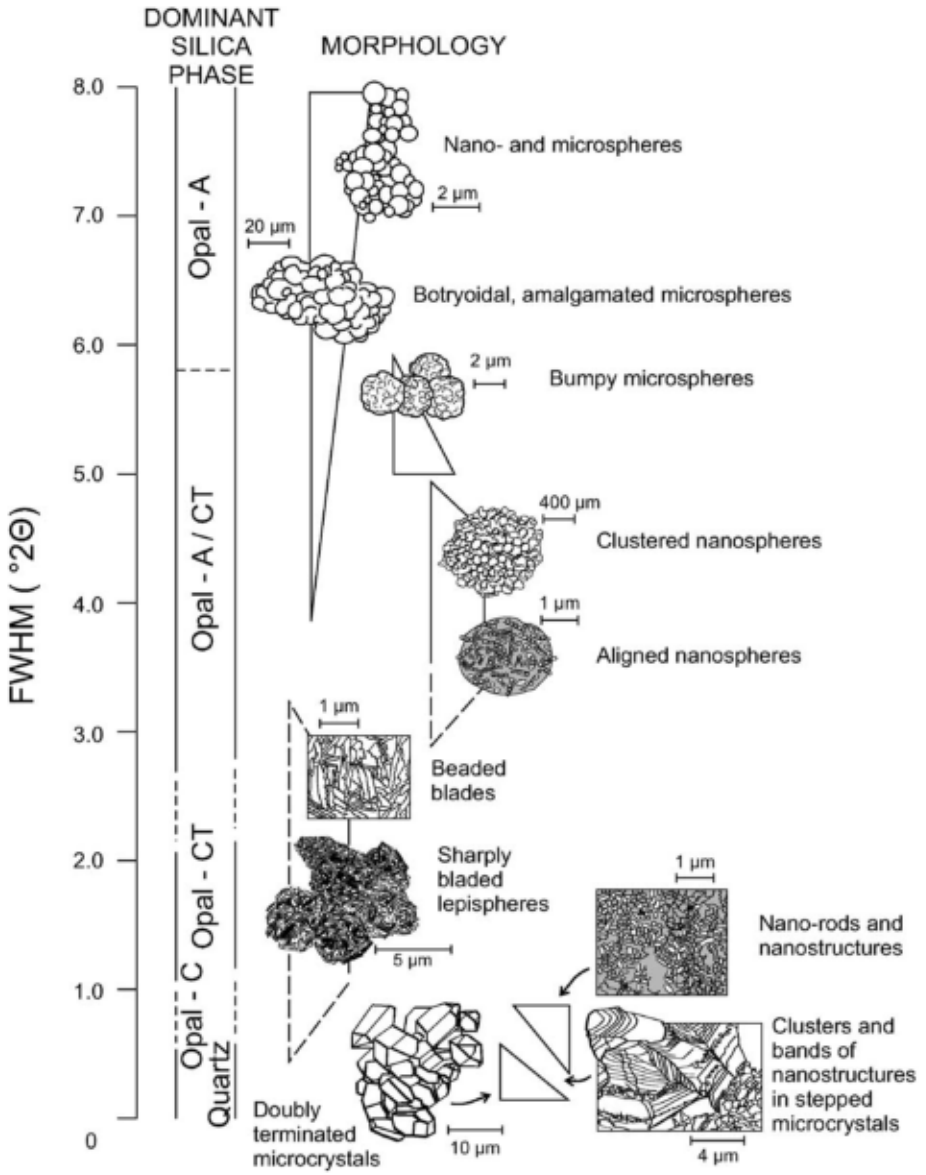

Fig. 3. Summary of morphologic changes that accompany dominant silica phase changes in the Opal Mound sinter. Transformation from one silica phase and morphological state to another occurs progressively and gradationally. Each stage overlaps the previous stage, resulting in the co-existence of two or more morphological states at any one point in the diagenetic pathway. Triangles schematically portray relative abundance of phases.

Moganite was detected within diagenetic quartz veins, but not in the opal-CT silica groundmass, wherever the FWHM values ranged from 2.3° to 1.3° 2θ. Moganite was also detected within the microcrystalline quartz groundmass of samples with FWHM values < 0.4° 2θ, but was not detected in cross-cutting fractures infilled with fibrous quartz or in fibrous quartz veins. Changes in quartz to moganite ratios were tracked across a vein of microcrystalline quartz in sample horizon AU55379, which yielded a FWHM value of 1.25° 2θ by XRPD analysis (Fig. 4E). The groundmass, on both sides of the vein (Fig. 4F), has

Table 3
Mineralogy of siliceous sinter samples from Opal Mound sinter deposit determined by X-ray powder diffraction analysis

AU number	Field number	Silica phase	Mineralogical group	Apex position (Å)	Maximum intensity (c/s)	FWHM (°2θ)	FWHM (Å)
55339	R1Ayellow	Opal-A	1	22.20	99	7.20	1.30
55340	R1Aorange	Opal-A	1	22.20	98	7.40	1.32
55341	R1Awhbrwn	Opal-A	1	22.10	99	7.30	1.28
55342	R1Atan	Opal-A	1	22.10	98	7.70	1.36
55351	R1Dtop	Opal-A	1	22.20	105	7.40	1.34
55352	R1Dmid	Opal-A	1	22.55	102	6.50	1.18
55353	R1Dbottom	Opal-A	1	22.05	98	7.10	1.30
55363	R1Iyellow	Opal-A	1	22.35	98	7.70	1.39
55364	R1Ibottom	Opal-A	1	22.10	102	7.45	1.39
55369	R1Mclear	Opal-A	1	22.10	107	7.15	1.31
55370	R1Mtan	Opal-A	1	21.80	110	6.45	1.16
55356	R1Fyellow	Opal-A	1	22.20	98	7.10	1.26
55357	R1Fblack	Opal-A	1	21.95	105	7.40	1.33
55358	R1Fwhite	Opal-A	1	22.35	100	7.40	1.34
55359	R1Fred	Opal-A	1	22.10	94	7.65	1.38
55360	R1Fbottom	Opal-A	1	22.40	106	7.05	1.28
55380	R6B	Opal-A	1	22.00	79	6.70	1.20
55354	R1E	Opal-A	1	22.20	83	7.35	1.39
55361	R1G	Opal-A	1	22.20	83	7.95	1.34
55366	R1K	Opal-A	1	22.30	83	7.40	1.30
55365	R1Iclear	Opal-A/CT	2	21.60	126	5.50	1.02
55344	R1Btan	Opal-A/CT	2	21.65	146	4.45	0.82
55344	R1Btan	Opal-A/CT	2	21.75	132	4.00	0.73
55344	R1Btan	Opal-A/CT	2	21.65	145	3.35	0.66
55344	R1Btan	Opal-A/CT	2	21.65	138	3.75	0.69
55344	R1Btan	Opal-A/CT	2	21.85	130	4.25	0.77
55344	R1Btan	Opal-A/CT	2	21.50	128	3.60	0.64
55344	R1Btan	Opal-A/CT	2	21.75	136	3.65	0.75
55344	R1Btan	Opal-A/CT	2	21.60	122	3.50	0.71
55344	R1Btan	Opal-A/CT	2	21.60	127	4.05	0.73
55344	R1Btan	Opal-A/CT	2	21.70	134	3.60	0.74
55345	R1Bclear	Opal-A/CT	2	21.55	171	3.75	0.71
55346	R1Bred	Opal-A/CT	2	21.55	176	3.50	0.67
55371	R1O	Opal-A/CT	2	21.65	113	4.55	0.79
55367	R1L	Opal-A/CT	2	21.60	126	5.55	1.02
55380	R6B2clear	Opal-A/CT	2	21.60	139	3.60	0.68
55381	R6B2	Opal-A/CT	2	21.60	202	2.70	0.51
55386	R8	Opal-A/CT	2	21.80	124	5.80	1.06
55395	R15	Opal-A/CT	2	21.75	100	4.60	0.83
55349	R1Cclear	Opal-CT+quartz	3	21.65	233	2.30	0.44
55348	R1Cwhite	Opal-CT+quartz	3	21.65	391	1.45	0.28
55348	R1Cwhite	Opal-CT+quartz	3	21.50	355	1.30	0.25
55348	R1Cwhite	Opal-CT+quartz	3	21.80	308	1.30	0.20
55348	R1Cwhite	Opal-CT+quartz	3	21.65	221	1.90	0.43
55348	R1Cwhite	Opal-CT+quartz	3	21.75	209	1.90	0.36
55348	R1Cwhite	Opal-CT+quartz	3	21.75	210	1.80	0.34
55348	R1Cwhite	Opal-CT+quartz	3	21.75	206	1.85	0.35
55348	R1Cwhite	Opal-CT+quartz	3	21.50	223	1.70	0.36
55348	R1Cwhite	Opal-CT+quartz	3	21.70	199	2.00	0.42
55348	R1Cwhite	Opal-CT+quartz	3	21.75	210	1.75	0.37
55377	R6A	Opal-CT+quartz	3	21.75	326	1.05	0.20

(continued on next page)

Table 3 (*continued*)

AU number	Field number	Silica phase	Mineralogical group	Apex position (Å)	Maximum intensity (c/s)	FWHM (°2θ)	FWHM (Å)
55378	R6aclvn	Opal-CT+quartz	3	21.75	323	1.50	0.23
55379	R6awhmog	Opal-CT+quartz	3	21.90	376	1.25	0.19
55384	R7vit	Opal-C+quartz	4	20.80	370	0.30	0.06
55384	R7vit	Opal-C+quartz	4	20.15	445	0.35	0.06
55384	R7vit	Opal-C+quartz	4	20.80	350	0.30	0.06
55384	R7vit	Opal-C+quartz	4	20.75	398	0.35	0.06
55384	R7vit	Opal-C+quartz	4	20.75	395	0.35	0.07
55384	R7vit	Opal-C+quartz	4	20.80	400	0.20	0.04
55384	R7vit	Opal-C+quartz	4	20.85	385	0.25	0.05
55384	R7vit	Opal-C+quartz	4	20.80	380	0.25	0.05
55384	R7vit	Opal-C+quartz	4	20.90	381	0.25	0.05
55384	R7vit	Opal-C+quartz	4	20.90	380	0.25	0.05
55385	R7porous	Opal-C+quartz	4	20.80	470	0.20	0.04
55387	R12	Opal-C+quartz	5	21.00	215	0.60	0.12
55373	R4	Quartz	5	21.00	345	0.35	0.06
55392	R14B	Quartz	5	21.00	420	0.32	0.06
55393	R14A	Quartz	5	21.00	498	0.25	0.05
55372	R3	Quartz	5	21.00	520	0.20	0.04
55375	R5b	Quartz	5	20.65	330	0.40	0.08
55376	R5c	Quartz	5	20.85	335	0.20	0.04
55388	R13(5)	Quartz	5	21.00	710	0.15	0.03
55389	R13(1)	Quartz	5	21.00	610	0.30	0.07
55390	R13(6)	Quartz	5	21.00	410	0.30	0.06
55391	R13(7)	Quartz	5	20.90	400	0.30	0.06

either a small amount of moganite (Fig. 4A) or none at all (Fig. 4B). Moganite peaks with higher maximum intensities were detected within the microcrystalline zone (Fig. 4C, D). Thus, moganite exists within microcrystalline zones in sinter which consist of opal-CT. Götze et al. (1998) evaluated the detection of moganite using Raman laser techniques and related the relative abundances of moganite and quartz to peak intensities. They showed that peak intensities were equal when a sample contained 80% moganite and 20% quartz (e.g., Fig. 4C). XRPD analysis of one moganite-rich sample AU55379 (Fig. 4C) revealed a small moganite peak at 26.3° 2θ, on the shoulder of the 26.68° 2θ quartz peak.

In summary, Raman laser microprobe analysis showed no moganite in samples with opal-A or opal-A/CT but it was present where opal-CT, opal-C and quartz occur. Moganite peak intensities are the highest in samples with opal-CT mineralogy but decrease where opal-C and quartz occur. This confirms moganite is a transitional phase in the process of sinter diagenesis and that quartz forms at the expense of moganite.

6.3. Physical characteristics of the sinter

The transformation in the physical characteristics of sinter during diagenesis can be followed by comparing sample density, porosity, Friability Index (FI) and retardation values (Table 5). Colored sinter from the Opal Mound consists of multiple, thin horizons (<2 mm) that could not be individually separated to measure their densities and porosities. Therefore, their measurements were made on bulk samples. However, it was generally possible to calculate a FI value of the individual colored horizons. FI analysis of the samples (Table 5) has not been particularly useful for characterizing sinters at Opal Mound because they are so well-indurated.

Regardless of location or their mineralogical maturation all samples have porosities of <15%. This contrasts with the work conducted on New Zealand sinters by Herdianita et al. (2000a), which revealed a decrease in porosity values with increasing maturation, as well as porosity values of opal-A of ~50%. Broadly, an increase in density values with silica phase maturation is recorded at Opal Mound and

Table 4
Results of 21 selected sites in eight samples from Opal Mound sinter analyzed by Raman laser microprobe for the presence of moganite

AU number	Sample	FWHM (°2θ)	Ratio moganite to quartz	Maximum intensity moganite cm^{-1}	Maximum intensity quartz cm^{-1}	Moganite peak position	Quartz peak position
55386	R8	5.80	–	–	–	–	–
55380	R6B01	3.60	–	–	–	–	–
55380	R6B02	3.60	–	–	–	–	–
55381	R6B202	2.70	–	–	–	–	–
55378	R6A02	1.50	–	–	–	–	–
55379	R6A01	1.25	1:2.4	7200	17200	502	464
55379	R6A03	1.25	1:1.1	7000	8000	501	464
55379	R6A05	1.25	1:1	10600	10500	501	465
55379	R6A04	1.25	1:18	100	1800	500	465
55348	R1C01	1.45	1:10	6000	60000	503	465
55348	R1C02	1.45	–	–	–	–	–
55384	R7void	0.30	1:12.3	2000	24500	502	464
55393	R14A03	0.25	1:9.7	5000	48500	504	465
55393	R14A02	0.25	1:38	2000	76500	503	465
55393	R14A04	0.25	1:108	500	54000	500	465
55393	R14A01	0.25	1:113	500	56500	500	465
55393	R14frac	0.25	–	–	22500	–	464
55393	R14fib	0.25	–	–	24500	–	464
55376	R501	0.20	1:13	4000	53000	503	465
55376	R502	0.20	1:22	2500	54500	502	465
55376	R5void	0.20	1:8.3	7000	58000	501	464

within New Zealand sinters. White, vitreous samples from the vent and near-vent areas at Opal Mound had the highest densities, with values greater than 2.50 g/cm^3. Samples from the mid-slope and distal-apron areas exhibited lower density measurements, ranging from 1.65 to 2.36 g/cm^3, with values variable from sample to sample.

6.4. Trace element composition

Eleven bulk samples were analyzed by XRF, and 13 individually selected horizons within six samples were analyzed by LA-ICPMS to determine their elemental concentrations within each sample. Samples for XRF analysis were specifically chosen to represent the range in color and silica mineral phase of white quartz to colored opal-A, from Opal Mound ridge to distal-slope sinter. Brightly colored samples were chosen for laser ablation analysis to determine whether any particular element was responsible for their strong coloration. Results are tabulated in Tables 6 and 7. XRF bulk analysis revealed relatively low As concentrations in sample AU55339 (2330 ppm); however, targeting of the yellow horizon within this sample by laser ablation revealed higher As concentrations (9423 ppm). XRF bulk analysis revealed high Al concentrations (1160 to 8210 ppm) in several distal-slope samples compared to the site-specific laser ablation method, which revealed 2 to 192 ppm Al, within the same samples. Laser ablation analysis detected lower Ca concentrations (<900 ppm) in colored sinter than was revealed by XRF analysis (<3500 ppm). Hence, individual sub-sample horizons selected for detailed study were unlikely to be layers which harbored high Al and Ca concentrations. The elemental compositions of the two vents differ. The northern vent (AU55389–AU55392) consists almost entirely of silica; whereas, the southern vent (AU55395) has appreciable Fe (1400 ppm), Mg (1200 ppm), Al (5600 ppm), K (1700 ppm) and Ca (1200 ppm). Variations in vent elemental concentrations suggest differences in discharging fluid compositions. At Opal Mound, only some colored samples preserve microbes, suggesting that biological activity did not influence trace element compositions. By comparing the results of the two analytical methods, it is evident that elemental concentrations within each sinter horizon are highly variable. Variability over small spatial distances is also observed in the mineralogy and morphology of the Opal Mound sinter deposit (Section 6.2).

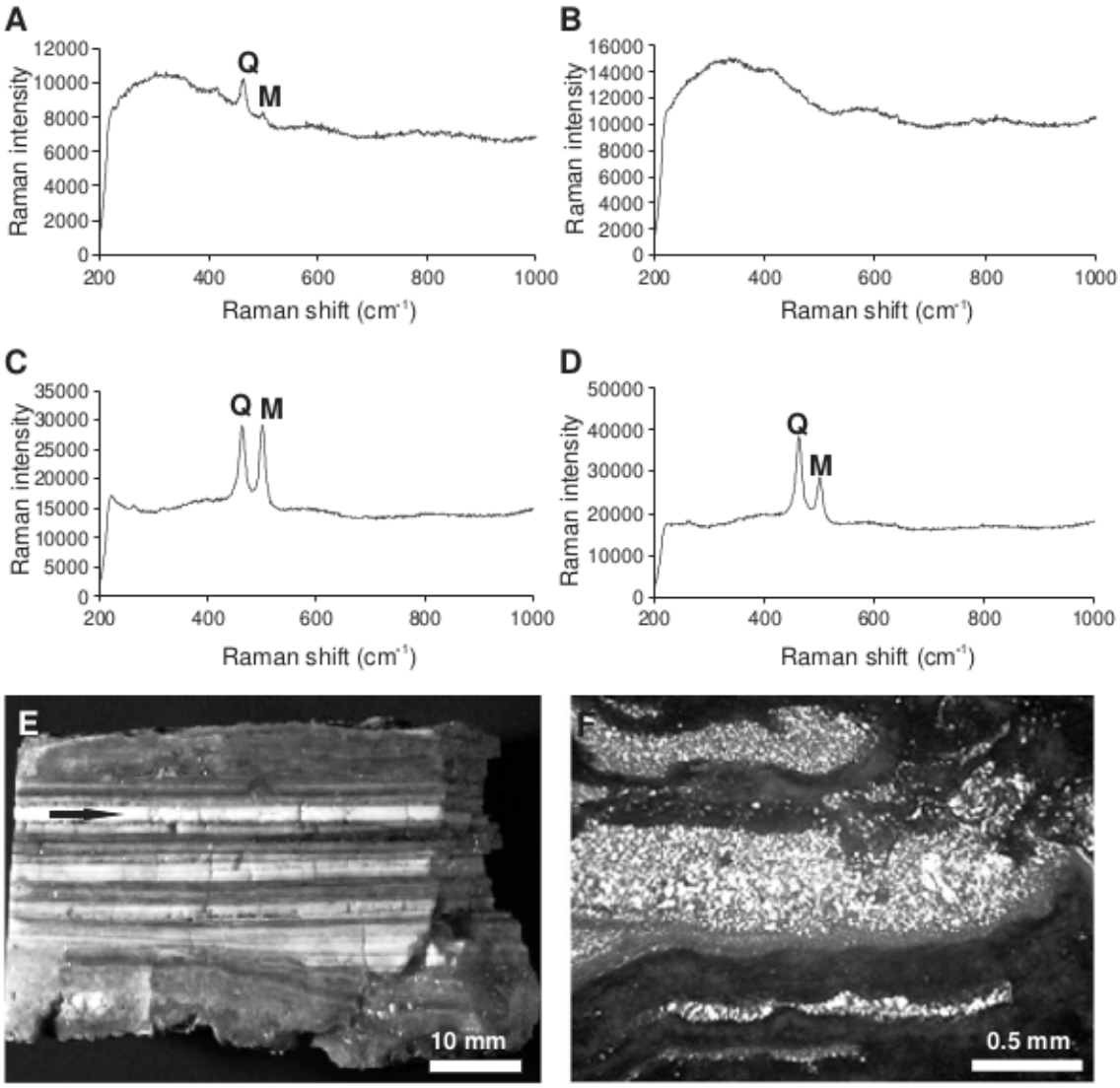

Fig. 4. Moganite detected by Raman laser microprobe analysis, in sub-sample AU55379 (FWHM value=1.25° 2θ), in bulk sample AU55377 (FWHM value=1.05° 2θ); Q=quartz; M=moganite. (A–B) Scan shows quartz but very little or no moganite in the fine-grained silica groundmass (black areas in F). (C–D) Moganite and quartz in the microcrystalline quartz zones (white areas in F). (E) Photograph of sample AU55377, with arrow indicating white horizon (AU55379), rich in moganite. (F) Thin section photomicrograph under crossed-polarized light of the white horizon shown in (E). Zones of fine-grained opal-CT appear as dark areas (moganite-poor), whereas microcrystalline quartz occurs as white speckled areas (moganite-rich).

In general, brightly colored sinters are not common in hot spring deposits. A few well-documented occurrences have been reported from several New Zealand sinter deposits (Parker and Nicholson, 1990; Jones et al., 1997; McKenzie et al., 2001), and at Steamboat Springs, Nevada, U.S.A (White et al., 1964). Documented XRF results on New Zealand sinters show elevated calcium, lower aluminum and comparable arsenic concentrations to Opal Mound sinter, while Steamboat Springs sinter has reportedly higher trace element concentrations than those found at Opal Mound.

Table 5
Physical properties of Opal Mound siliceous sinter samples including density, porosity, friability index and retardation values

AU number	Sample number	Porosity ± 1.0 (%)	Density ± 0.04 (g/cm3)	Friability index (±0.02)	Retardation of quartz (± 0.005)
55339–55342	R1A	12.95	2.36	2.76–9.07	–
55344–55346	R1B	8.0	1.98	4.1–25.4	–
55348–55349	R1C	1.0	1.81	0.25	–
55351–55353	R1D	12.0	1.83	0.26	–
55354	R1E	6.0	1.95	1.55	–
55356–55360	R1F	8.0	1.65	8.0	–
55361	R1G	4.0	2.02	–	
55363–55365	R1I	7.7	2.05	2.39	–
55366	R1K	10	1.75	2.95	–
55367	R1L	2.0	2.0	12.7	–
55369–55370	R1M	4.0	2.31	7.9	–
55371	R1O	2.05	13.3	9.77	–
55372	R3	4.0	2.34	12.7	–
55373	R4	2.4	2.21	12.9	0.0
55375–55376	R5	10.0	2.64	12.7	0.04
55377–55379	R6A	7.0	2.19	12.7	0.04–0.05
55380	R6B	4.0	2.49	3.97	–
55381–55382	R6B2	2.0	2.10	12.7	
55384–55385	R7	3.0	1.93	63.5	0.003–0.007
55386	R8	1.0	2.04	42.3	–
55387	R12	15.0	1.85	–	
55388–55391	R13	9.0	2.98	4.7	–
55393	R14A	14.0	2.50	1.79	–
55392	R14B	6.0	2.51	63.5	0.01–0.05
55395	R15	10.0	1.92	18.14	–

6.5. Microbial textures

Filamentous microbes thrive in modern hot springs and many become entombed in sinter deposits. Because different taxa dominate particular environments, they can be useful paleoenvironmental indicators. The morphological terminology of sinter microbial macrostructures and preserved microtextures has been outlined in various reports (Cassie, 1989; Merz, 1992; Cady and Farmer, 1996; Walter et al., 1996; Jones et al., 1997, 2001; Lowe et al., 2001; Guidry and Chafetz, 2003b, 2003c; Lynne and Campbell, 2003). Broad sub-environments such as high, mid, or low temperature can sometimes be inferred from the preserved textures, specifically using filament sheath and trichome diameters, if sheathed microbes are present and unaltered by diagenesis (Cady and Farmer, 1996; Walter et al., 1996; Lowe et al., 2001; Lynne and Campbell, 2003). For example, mid-range thermal conditions (~35–60 °C) are indicated by trichome diameters of 2–3 μm, and exterior sheath diameters of ~5 μm. Trichome diameters of >5 μm and exterior sheath diameters >10 μm are attributed to low-temperature (<35 °C) microbes. Coarsely filamentous microfossils dominate the distal-slope sinters at Opal Mound (Fig. 5A, B), suggesting that they were deposited by cool fluids. Nonetheless, some horizons contain finely filamentous microbes indicative of mid-temperature environments (Fig. 5C, D). One filament in Fig. 5C exhibits a hollow trichome (0.5 μm diameter) while the other is infilled with homogeneous silica. Some filamentous horizons consist of clusters of bushy filaments, such as those shown in sample AU55339 (Fig. 5D) from the distal slope area. Numerous distal slope samples preserve streamer fabrics of elongated filaments to 8 mm in length, which are inferred to have formed in fast-flowing water (Fig. 5E, F). Preservation of both low- and mid-temperature microbes at Opal Mound implies fluctuating discharge temperatures, flow rates, and/or changes in locations of the vents. For example, distal slope sample AU55358 contains filamentous microfossils (Fig. 5C) with exterior sheath diameters of 4 μm, typical of mid-temperature microbes. The loss of an identifi-

Table 6
Composition of selected bulk samples determined by X-ray fluorescence analysis, expressed as weight percent

Compound	LLD	R13	R6A	R6B	R6B2	R15	R5	R1A	R1C	R1E	R1B	R1F
		Vent	Mid-slope	Mid-slope	Mid-slope	Vent	Near vent	Distal slope	Distal slope	Distal slope	Distal slope	Distal slope
Na_2O	0.0054	bd	0.20	0.140	0.17	0.120	bd	0.130	0.140	0.140	0.094	0.061
		bd				0.097			0.120			0.042
Al_2O_3	0.0060	0.052	0.554	0.034	0.035	0.564	0.038	0.821	0.342	0.116	0.354	0.445
		0.066				0.564			0.320			0.441
SO_3	0.0081	0.017	0.024	0.058	0.30	0.086	0.079	0.566	0.039	0.421	0.19	0.212
		0.18				0.064			0.022			0.181
MgO	0.0020	bd	0.046	bd	bd	0.130	bd	0.07	bd	bd	bd	0.044
		bd				0.110			bd			0.045
K_2O	0.084	0.045	0.239	0.102	0.125	0.188	0.045	0.209	bd	0.125	0.092	0.099
		0.042				0.169			0.79			0.095
CaO	0.0064	0.014	0.344	0.052	0.098	0.126	0.062	0.088	0.080	0.06	0.034	0.037
		0.012				0.120			0.066			0.034
Fe_2O_3	0.0080	0.008	0.080	0.011	0.008	0.148	0.008	0.156	0.022	0.041	0.023	0.122
		0.008				0.139			0.021			0.117
MnO	0.0040	bd	0.061	0.005	0.013	0.009	bd	0.004	0.007	bd	bd	bd
		bd				0.009			0.005			bd
P_2O_5	0.0270	bd	bd	0.027	bd	0.027	bd	bd	bd	bd	bd	bd
		bd				0.028			bd			bd
Cl	0.0092	bd	bd	bd	bd	bd	0.016	bd	0.069	bd	bd	bd
		bd				bd			0.052			bd
Cr	0.0020	bd	0.002	bd	bd	bd	bd	0.002	bd	bd	0.002	bd
		bd				bd			0.003			bd
Co	0.0025	0.018	bd	0.007	0.010	0.004	0.025	0.0.09	0.002	0.018	0.003	bd
		0.019				0.003			bd			0.01
Cu	0.0016	0.003	0.003	0.003	bd	0.003	0.002	0.004	0.003	0.003	0.004	0.003
		0.003				0.002			0.002			0.003
Tl	0.0048	bd	0.009	0.006	0.029	bd	bd	0.008	bd	0.024	0.097	0.018
		bd				bd			bd			0.016
TiO_2	0.0039	bd	0.016	bd	bd	0.026	bd	0.021	bd	bd	bd	bd
		bd				0.023			bd			0.016
Ga	0.0016	0.003	0.009	bd	0.002	0.002	bd	bd	0.003	bd	0.002	bd
		0.003				0.002			0.002			bd
Sb	0.0040	0.11	bd	0.039	0.155	bd	0.021	bd	0.039	0.142	0.512	0.102
		0.011				bd			0.028			0.090
As	0.0039	bd	bd	bd	0.013	bd	bd	0.233	0.019	0.084	0.68	0.031
		bd				bd			bd			0.029
Rb	0.0008	bd	0.004	0.002	0.003	0.002	bd	0.003	0.002	0.002	0.002	0.001
		bd				0.002			0.002			0.001
Sr	0.0035	bd	0.005	bd	bd	bd	bd	bd	bd	bd	bd	bd
		bd				bd			bd			bd
SiO_2	0.0007	99.57	98.41	99.42	98.94	98.47	97.37	97.74	99.13	98.76	98.11	98.75
		99.61				98.62			99.26			98.84

Lower limit of detection (LLD) is approximate as limits vary slightly within individual samples. (bd=below detection limit).

able trichome in sample AU55358 with opal-A mineralogy shows that diagenesis occurs in patches and can destroy biosignals in even mineralogically immature sinter (cf. Lynne and Campbell, 2003). Jones et al. (2004) reported that taxonomic fidelity of silicified cyanobacteria can be compromised during the diagenesis from opaline silica to microcrystalline quartz, which commonly leads to degradation of the microbes and loss of taxonomically important features. Because silica infill and diagenesis can eradicate micron-scale

Table 7
Laser ablation results (ppm) of trace elements in different colored horizons of samples AU55338–AU55346, distal sinter apron

Element	Tan AU55342		Yellow AU55339		Orange AU55340	Clear AU55345		Red AU55346		Tan AU55344		Tan AU55344	
Be	0.99	0.2	2.3	2.2	1.1	109	139	21	8.7	0.99	2.03	19	7.2
B	146	263	76	73	182	36	65	91	209	60	10	14	20
Mg	5.9	2.7	4.5	5.3	2.2	4.7	18	7.7	10	1.0	4.7	2.1	1.9
Al	37	2.6	17.4	17	4.2	68	192	10.7	67	3.65	26.7	36	7.7
P	8.8	4.9	11.5	11.4	6.8	6.0	5.9	5.5	5.5	4.9	10.6	5.7	5.2
Ca	182	588	115	71	151	260	892	453	895	247	214	158	155
Ti47	2.1	1.5	1.9	1.6	1.5	0.9	0.8	0.8	0.8	0.8	1.7	0.8	0.7
Ti49	0.9	0.5	0.9	0.7	0.5	1.2	1.45	0.6	0.4	0.4	1.3	0.5	0.4
V	12	4.4	5.9	5.0	9.0	6.1	13.4	12	7.6	1.6	2.2	1.9	1.4
Mn	0.9	9.5	0.3	0.3	1.5	33.5	280	61	128	9.2	16.3	39.8	26.7
Cu	0.3	bd	0.9	0.9	bd	0.02	bd	0.03	bd	0.03	0.4	bd	bd
Zn66	0.78	bd	4.9	6.3	0.2	0.82	0.35	0.08	0.02	0.06	2.3	0.06	0.05
As	333	31	9423	6145	97	4.4	3.0	5.5	31	3.3	21	2.0	2.1
Rb	22	53	11	11	36	13.9	25.6	26	51	17.3	3.2	4.4	5.1
Sr	5.8	21	4.2	3.2	7.3	5.1	16	11	25	8.26	4.1	3.2	3.0
Ba	0.77	0.53	13.7	15.5	0.21	0.1	0.3	0.22	0.054	0.18	0.36	0.06	0.06
Pb	0.058	0.007	0.23	0.113	0.0128	0.007	0.005	0.003	0.001	0.004	0.057	bd	bd
Fe	bd	bd	bd	bd	bd	bd	bd	bd	bd	bd	bd	bd	bd
Si	377369	377369	381590	381590	372054	380890	382666	381579	375310	381579	381579	385759	380529

For each color, two separate sites were analyzed (bd=below detection limit).

microbial textures, other sedimentologic, stratigraphic, and paleontologic evidence should be sought to assess sinter-slope position and broad paleotemperature gradients in ancient sinters (cf. Campbell et al., 2001, 2004).

6.6. Morphological changes accompanying silica diagenesis

6.6.1. Overview

Progressive morphological transitions at nano- to micron-scales accompany the mineralogical shift from opal-A to quartz at Opal Mound (Table 3, Figs. 2 and 3). Five incremental steps in morphology occur in temporal sequence: (1) opal-A microspheres; (2) aligned opal-A/CT nanospheres; (3) opal-CT bladed lepispheres; (4) opal-C nano-rods; and (5) blocky quartz microcrystals that develop into doubly-terminated, quartz crystals. As diagenesis proceeds, a repetitive pattern of growth and shrinkage occurs in silica particle sizes (Fig. 3). Initially, 8 μm diameter opal-A microspheres transform into ~200 nm diameter bumpy, nanospheres, which subsequently become smooth and aligned into rows. These nanospheres then grow into 5 μm diameter opal-CT lepispheres before shrinking in size and changing shape to ~ 200 nm sized, opal-C nano-rods. In the final stage, these nano-rods of opal-C transform into blocky nanostructures prior to quartz crystal formation.

6.6.2. Microspheres (opal-A)

Silica nanospheres are not present in 1600 year old opal-A sinter at Opal Mound because it has already progressed a short distance down the diagenetic path during early aging, to botryoidal microspheres (Fig. 3). Based on previous studies of newly deposited sinter (e.g., Fig. 6A) by Smith et al. (2003), it is assumed that opal-A nanospheres were the precursor to the opal-A microspheres now found at Opal Mound. Individual opal-A spheres up to 8 μm in diameter form botryoidal clusters (Fig. 6B). At Opal Mound, this morphology correlates with FWHM values between 7.7° and 5.8° 2θ. In this early phase sinter, all opal-A spheres are cemented together in a smooth silica matrix. This ubiquitous, somewhat dense matrix coating is most likely the reason for the lower than expected porosities of <13% and densities of up to 2.36 g/cm^3 at Opal Mound (cf. Herdianita et al., 2000a). In the next diagenetic step, some samples with mineralogically more mature opal-A/CT (see Section 6.6.3 below) also contain some remnant

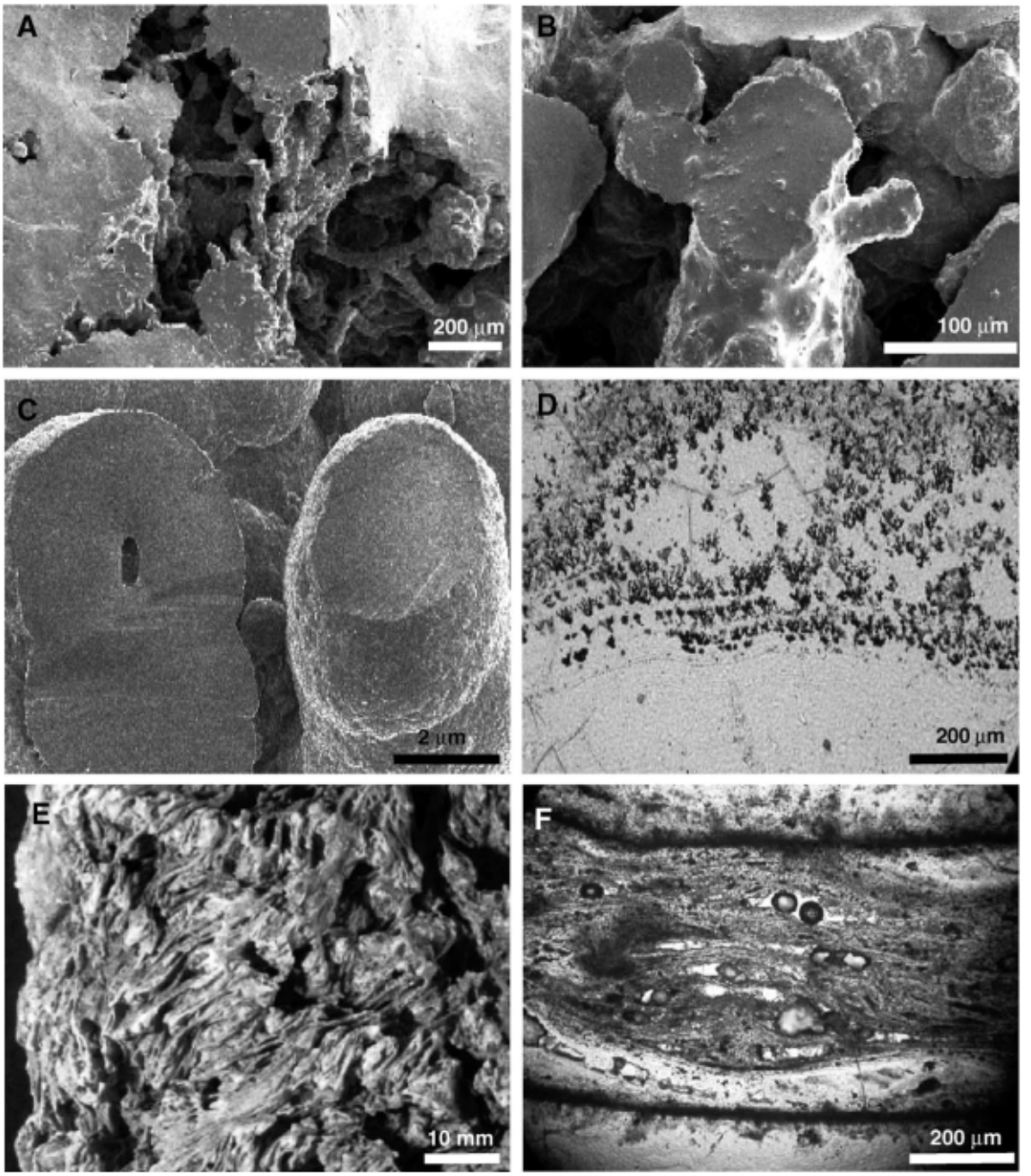

Fig. 5. Preserved microbial textures in distal-slope sinter at Opal Mound. (A–C) SEM images. (A) Overview of coarse filaments inferred to represent low-temperature microbes. AU55339. (B) Detail of microfossils shown in (A); filaments are infilled with silica. (C) Two filaments measuring 4 μm in exterior diameter, inferred as silicified mid-temperature microbes. Left microfossil reveals internal mold (0.5 μm in diameter), whereas the other is entirely infilled with silica. Sample AU55358. (D) Thin section photomicrograph show clusters of bushy filaments in plane-polarized light from a yellow colored, As-rich horizon. AU55356. (E) Hand specimen photograph of upper surface of sinter showing silicified elongated microbes parallel to the ground surface. Sample AU55356. (F) Thin section photomicrograph under plane-polarized light of elongate microfossils shown in (E).

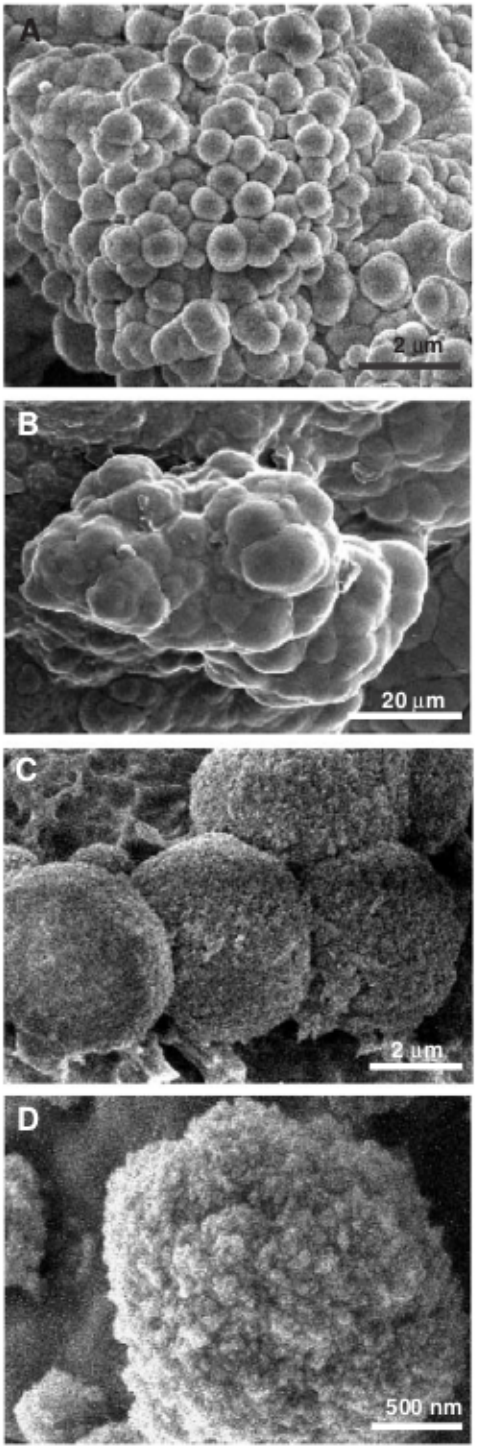

botryoidal clusters of opal-A spheres. Hence, there is a morphological overlap between these two early diagenetic mineralogical categories.

6.6.3. Bumpy spheres and aligned nanospheres (opal-A/CT)

The opal-A/CT group displays a range in FWHM values from 5.8° to 2.7° 2θ. Morphologic changes in the microstructure are initiated by an increase in "bumpiness" of the once smooth opal-A spheres (Figs. 3 and 6C, D). With a further decrease in FWHM values to 4.6° 2θ, the bumps decrease in size and reorganize into clusters of smooth nanospheres (Figs. 3 and 7), which subsequently align into rows. Each elongated set of aligned nanospheres measures 0.5 to 1.0 μm long and <0.2 μm wide, and is randomly oriented with respect to its neighbors. The aligned spheres occur in two different sizes, measuring 100–125 nm or <25 nm in diameter. It is common for the two nanosphere-sizes to be present within a single siliceous horizon and for different sized nanospheres to form from, and to coat the surface of previously formed opal-A spheres. Here, morphologic transformation of opal-A to opal-CT occurs in spatially minute increments. Some samples (e.g., AU55346) reveal smooth, opal-A botryoidal clusters co-exist with newly aligned nanospheres. Classic bladed lepispheres typical of opal-CT morphology do not begin to form until FWHM values drop to <4.45° 2θ (step 3, Section 6.6.4).

6.6.4. Bladed lepispheres (opal-CT+quartz)

The development of classic opal-CT bladed lepispheres (AU55348–AU55349, AU55377; Fig. 2C) occurs when aligned nanospheres of opal-A/CT join to form beaded, somewhat jagged plates (Figs. 3 and 8A). The newly formed opal-CT lepispheres initially

Fig. 6. Early transformation from opal-A microspheres to opal-A/CT at Opal Mound involves the formation of nanospheres from microspheres of silica. (A–D) SEM images. (A) The initial morphology of sinter may be clusters of opal-A spheres up to 1 μm diameter and is the presumed initiation point for Opal Mound diagenesis although not actually present. Sample from freshly deposited sinter in the Wairakei discharge drain, New Zealand. (B) Botryoidal clusters of smooth opal-A microspheres, up to 8 μm in diameter. Sample AU55340 (FWHM value=7.4° 2θ). (C–D) Irregular, knobby surfaces of opal-A spheres (2 μm in diameter). Sample AU55386 (FWHM value=5.8° 2θ).

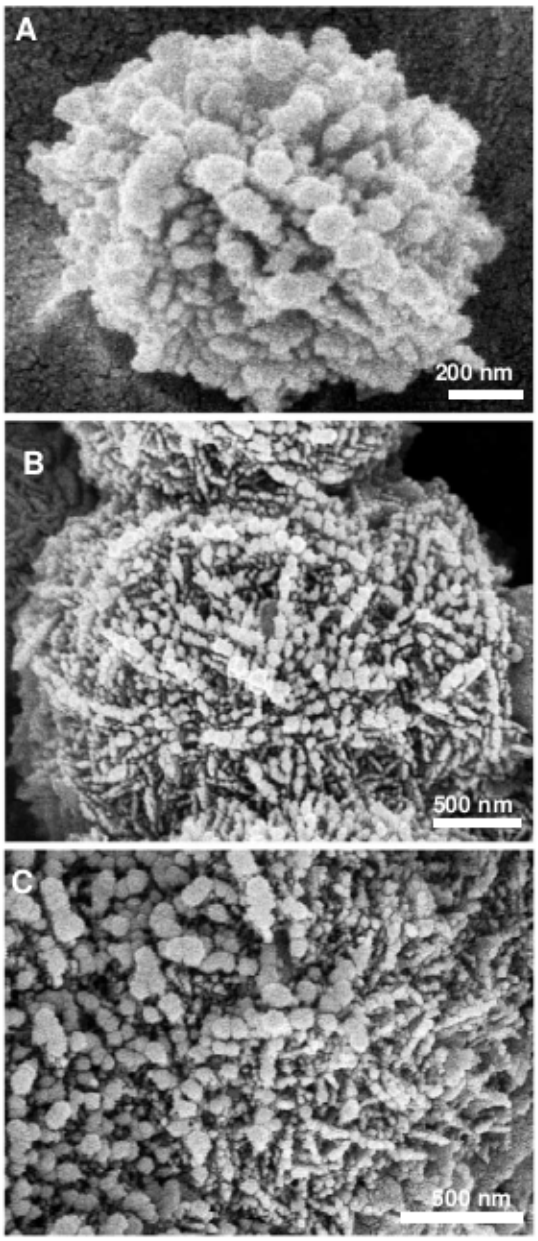

Fig. 7. Reorganization of opal-A/CT spheres to opal-CT bladed lepispheres begins with the alignment of nanospheres (<125 nm in diameter) into rows, each of which is randomly oriented within and around the microsphere. Sample AU55345 (FWHM value=3.75° 2θ). (A–C) SEM images. (A) One sphere showing randomly oriented rows of aligned nanospheres (<100 nm in diameter). (B) Oriented rows of sub-aligned nanospheres (<125 nm in diameter) cover a remnant opal-A sphere (2.5 μm in diameter). (C) Detail of (B) showing that aligned nanospheres are of different sizes.

retain an open structure composed of randomly oriented blades (Fig. 8B) which become more sharply bladed. The FWHM values of these samples range between 2.30° and 1.05° 2θ. Upon further maturation to opal-C+quartz (step 4, Section 6.6.5), the "classic" opal-CT bladed lepispheres lessen in abundance, occurring only as a minor component in the matrix. However, their presence indicates that the morphological transformations occur gradually and follow the mineralogical changes.

6.6.5. Nano-rods and clustered nanostructures (opal-C+quartz)

A major morphological change is recorded in the opal-C to quartz samples (AU55387, Fig. 2D; AU55384) with FWHM values of 0.6° to 0.2° 2θ. In particular, restructuring from opal-CT bladed lepispheres to opal-C morphology involves the reorgani-

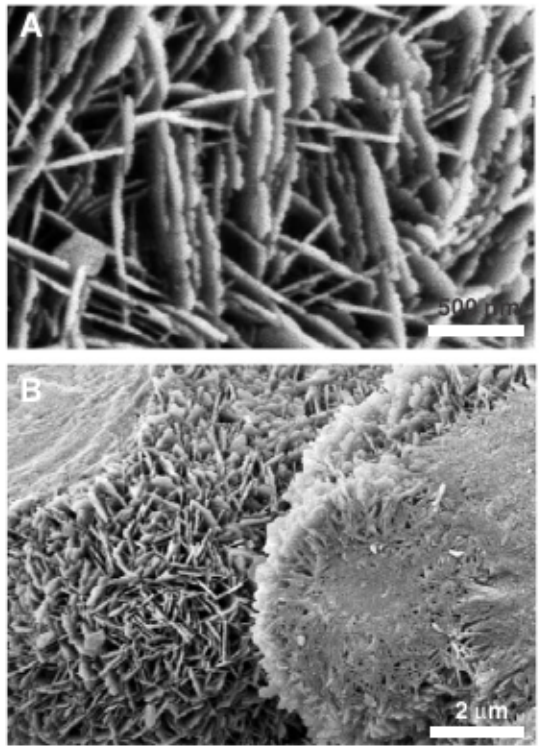

Fig. 8. Microstructures of incipient to well-developed opal-CT (FWHM value=2.3° 2θ). Sample AU55349. (A–B) SEM images. (A) Open network of early opal-CT lepisphere formation shows that upper blade surfaces are jagged, comprising merged remnants of aligned opal-A nanospheres. (B) Variably oriented, sharp opal-CT blades.

zation of blades into elongate, randomly oriented, 200 nm long clusters of nano-rods (Figs. 3 and 9A, B) or blocky nanostructures (Fig. 10F). Some samples also display patches of microcrystalline quartz (Fig. 9C–F). Quartz crystals growing into voids exhibit c-axes oriented approximately parallel to the void rim, are

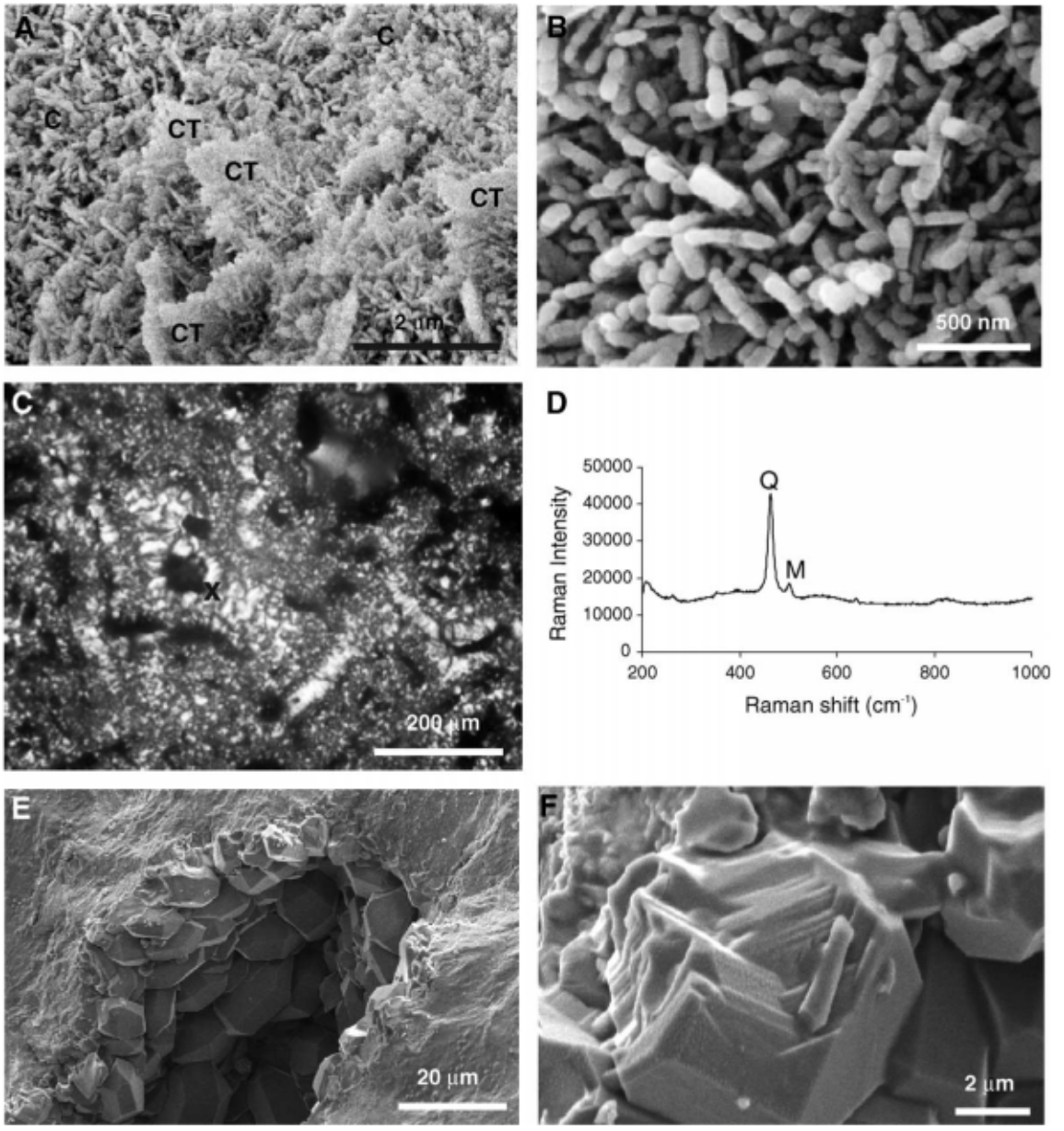

Fig. 9. Morphologic changes occurring during the transformation of opal-CT to opal-C + quartz (FWHM values = 0.6° to 0.35° 2θ). (A–B) SEM images of sample AU55387. (A) Remnant opal-CT bladed lepispheres (CT) in a groundmass of opal-C (C). (B) Detail of opal-C groundmass in (A) showing rectangular nano-rods (arrows), dominantly 200 nm in length. (C–F) Sample AU55384. (C) Thin section photomicrograph under cross-polarized light indicating that diagenetic quartz has pseudomorphed opal-C. x = Raman microprobe scan site. (D) Raman microprobe scan of quartz and moganite in the groundmass shown in (C). (E) SEM image showing doubly terminated quartz crystals growing with their c-axes parallel to the cavity walls. (F) SEM image showing the stepped surfaces of a growing quartz crystal.

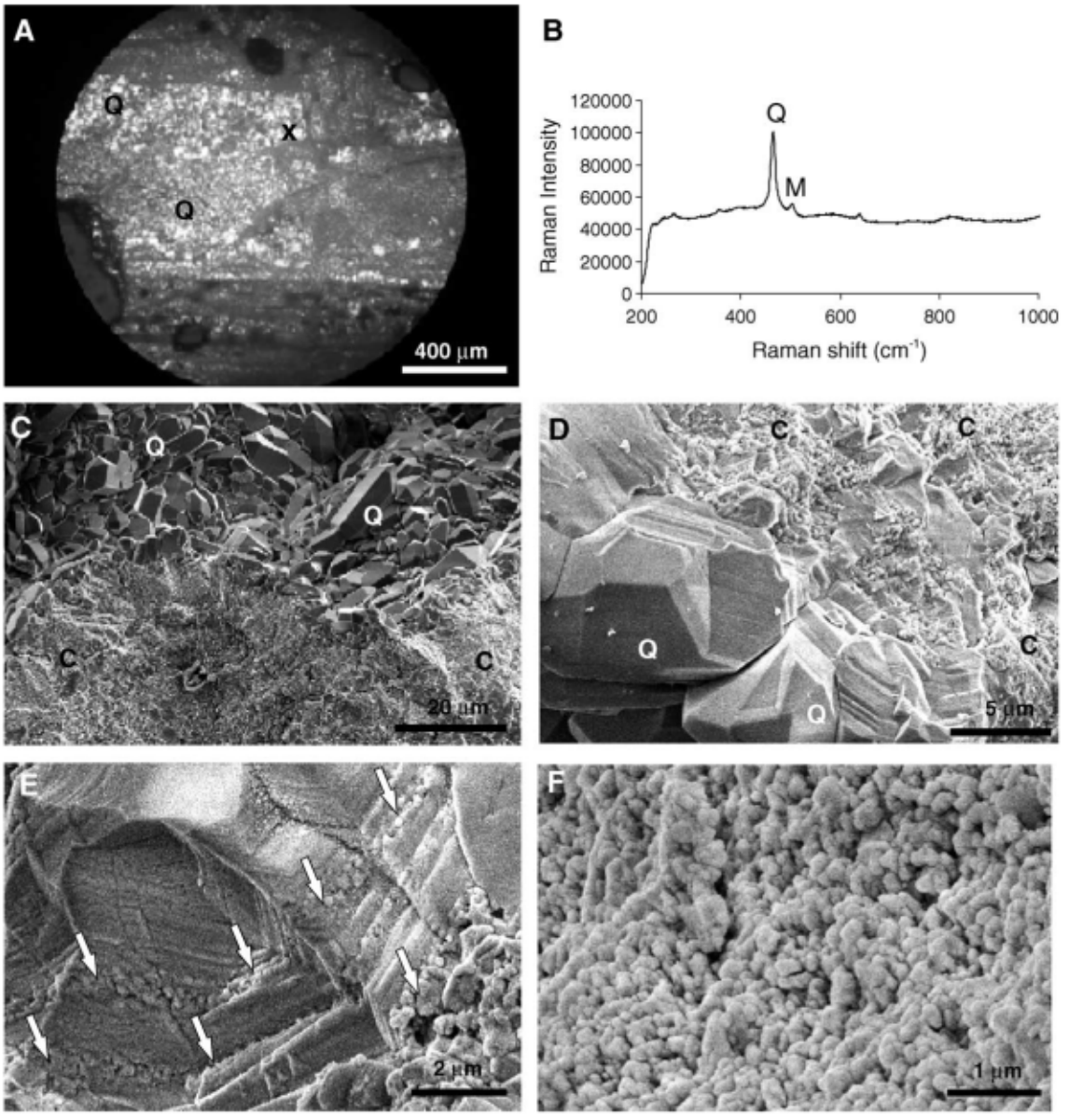

Fig. 10. Quartz mineralogy reveals quartz microcrystal formation and remnant opal-C morphology. (A) Thin section photomicrograph of diagenetic microcrystalline quartz (Q) under cross-polarized light. x=Raman microprobe scan site. Sample AU55392 (FWHM=0.32° 2θ). (B) Raman scan detected both quartz and moganite in the microcrystalline groundmass shown in A. (C–F) SEM images. (C) Groundmass of sample AU55375 (FWHM=0.4° 2θ), showing transformation to quartz crystals (Q) oriented parallel to the sinter surface, in a groundmass of opal-C (C). (D) Diagenetic quartz (Q) crystals with stepped faces. Numerous opal-C nanostructures (C) occur at the base of the quartz crystals and in the groundmass. (E) Detail of stepped surfaces in (D) shows that steps consist of bands of nanostructures (arrows) which are separated by smooth steps of quartzose silica. (F) Detail of opal-C nanostructures (in D and E) showing equant to elongate clusters of nanostructures up to 200 nm long.

doubly-terminated, and up to 25 μm long (Fig. 9E). Steps on some crystal faces reflect the progressive growth of the quartz (Fig. 9F).

6.6.6. Banded nanostructures and microcrystals of quartz (quartz)

Two types of quartz crystals occur at Opal Mound — diagenetic and fibrous hydrothermal (see Section 6.6.7) — each representing a different generation of quartz formation. Diagenetic quartz crystals develop with c-axes parallel to the sinter surface, and are formed in the groundmass or in voids (Figs. 9C–F and 10). This type of quartz forms from gradual restructuring of opal-C nano-rods and clusters of blocky nanostructures (Figs. 9B and 10F). The restructuring is visible either at the base of growing quartz crystals (Fig. 10D–F) or in the groundmass (Figs. 10C, D and 11A, B). Moganite was detected with diagenetic quartz (Figs. 9D, 10B and 11D), but not with hydrothermal quartz (Fig. 12B, D).

The northern vent, near-vent and some mid-slope samples yielded XRPD traces with quartz but none was detected in the southern vent, some of the mid-slope samples, or in any of the distal slope samples. This quartz distribution suggests two distinct pulses of thermal fluids. The first pulse emanated from the northern vent depositing sinter along Opal Mound ridge, which has diagenetically altered to quartz. The second fluid pulse from the southern vent created the colorful distal slope sinter and infilled fractures within the older sinter deposit. The distribution of quartz is consistent with the fact that the northern vent comprises mostly silica (99.6%) and is mature (FWHM=0.3° 2θ), whereas the southern vent has higher concentrations of trace elements and is immature (FWHM=4.6° 2θ).

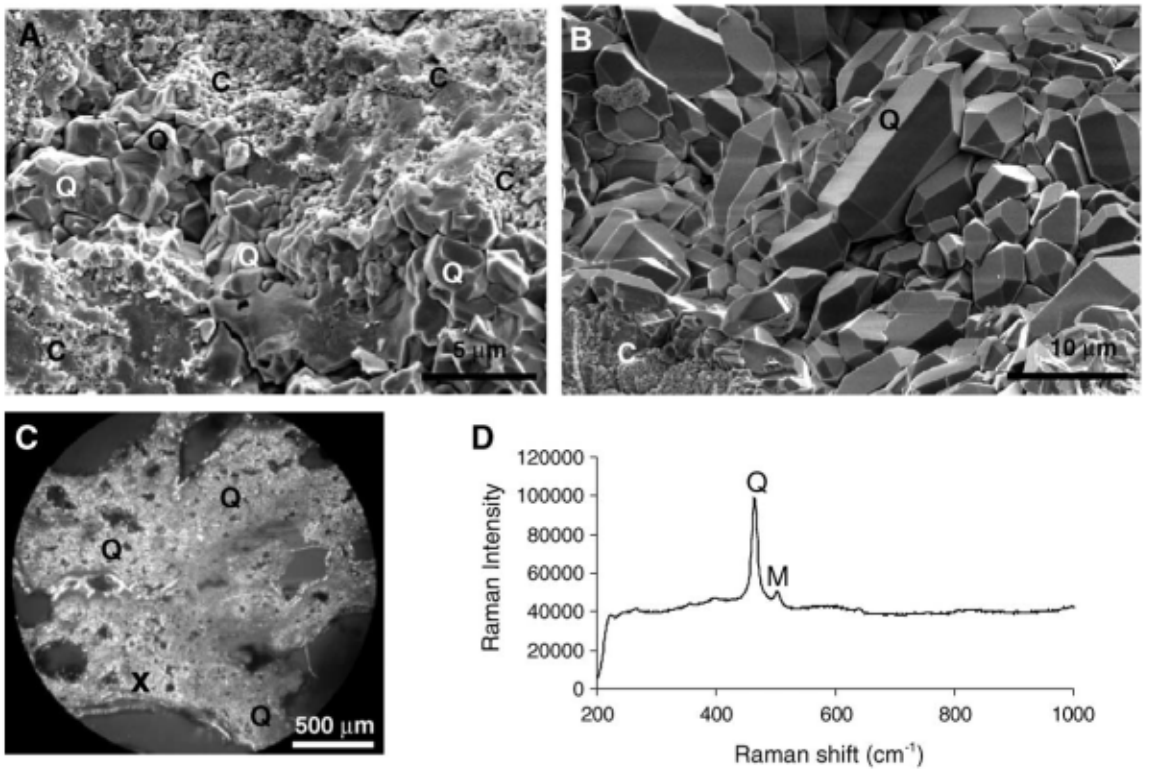

Fig. 11. Opal-C nanostructures (C) and doubly-terminated diagenetic quartz crystals (Q). Sample AU55376 (FWHM value=0.2° 2θ). (A–B) SEM images. (A) Quartz crystals within a groundmass of opal-C. (B) Smooth, doubly-terminated quartz crystals in the groundmass, with c-axes parallel to the sinter surface. Opal-C nanostructures surrounding quartz crystals shown in lower left. (C) Thin section photomicrograph shows the groundmass to consist of densely-packed, microcrystalline diagenetic quartz. Cross-polarized light. x=Raman microprobe scan site. (D) Raman microprobe scan of microcrystalline quartz groundmass shown in (C), documenting the presence of quartz and moganite.

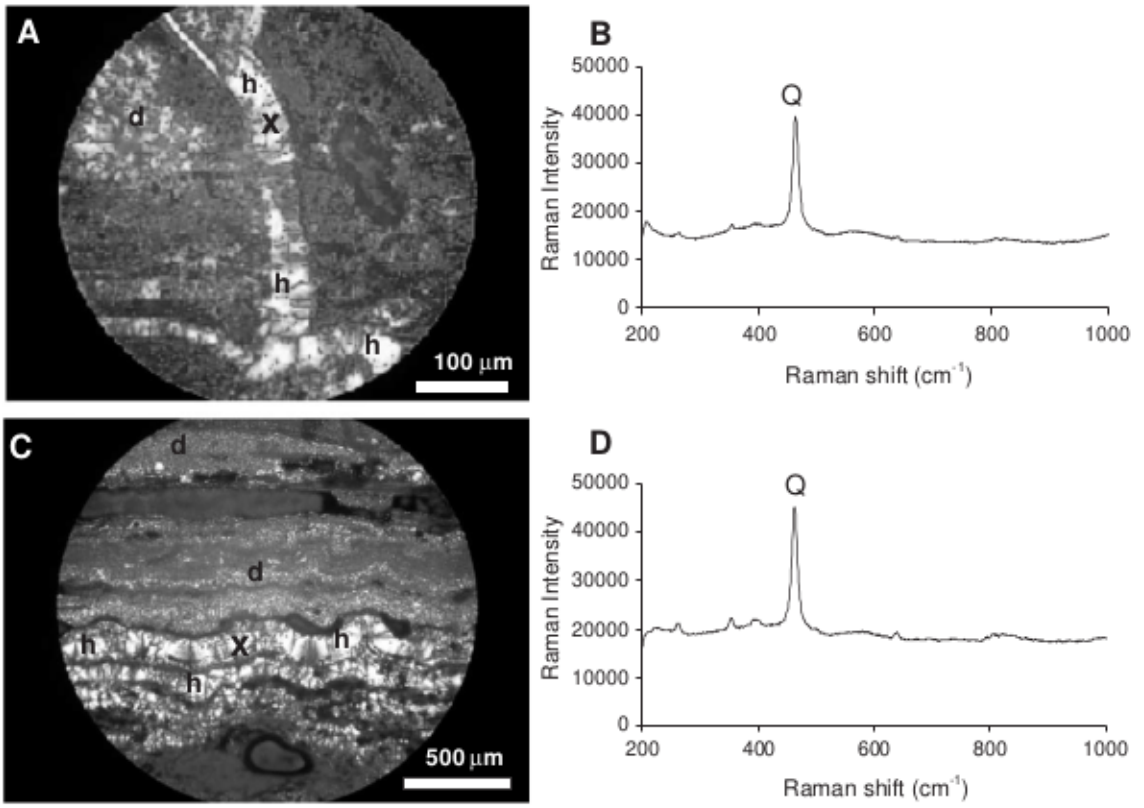

Fig. 12. Late-stage, fibrous hydrothermal quartz filling fractures, and undulose fibrous veins cross-cutting the groundmass of diagenetic quartz. (A, C) Photomicrographs of hydrothermal (h) and diagenetic (d) quartz (sample AU55392, FWHM=0.32° 2θ). (A) Fracture infilled with hydrothermal quartz cross-cutting a groundmass of diagenetic quartz; x=site of Raman microprobe scan shown in (B). (B) Raman microprobe scan of quartz-filled fracture. Moganite is not present. (C) Undulose zones of fibrous, late-stage hydrothermal quartz, cutting through a groundmass of diagenetic quartz; x=site of Raman microprobe scan shown in (D). (D) Raman microprobe scan of fibrous hydrothermal quartz. No moganite is present.

6.6.7. Late quartz veins and infill

In contrast to diagenetic quartz, fibrous late-stage hydrothermal quartz crystals lack moganite, and occur as fracture infill within the deposit, growing perpendicular to the void or fracture rims (Fig. 12). Some samples contain both types of quartz, typically where the groundmass comprises diagenetic quartz (Figs. 10 and 11) and the infilled fractures contain fibrous hydrothermal quartz (Fig. 12). Ten of the sub-samples yielded quartz XRPD traces. These showed FWHM values ranging from 0.4° to 0.15° 2θ.

Sample AU555348 (opal-CT+quartz) contains voids infilled with microcrystalline silica geopetals (Fig. 13A). Other voids are partially infilled with quartz crystals, which decrease in size and grade into microcrystalline quartz away from the open void (Fig. 13B). Some microcrystalline quartz-filled fractures are micro-faulted (Fig. 13C). Thin section microscopy and XRPD analysis indicate that the microcrystalline quartz in voids and veins shown in Fig. 13C–D, occur within a groundmass of fine-grained opal-CT silica. It is likely that these quartz-infilled fractures, voids and veins are responsible for the quartz peak on the XRPD traces of samples with opal-CT mineralogy. Moganite was detected (Fig. 13E, F) within microcrystalline quartz veins of mid-slope samples (AU55349, AU55379) with opal-CT+quartz mineralogy. The mid-slope samples with veins and fracture infill (Fig. 13) differ from the Opal Mound ridge samples that also display fracture infill (Fig. 12) in that there is no evidence of moganite within the veins of the ridge samples.

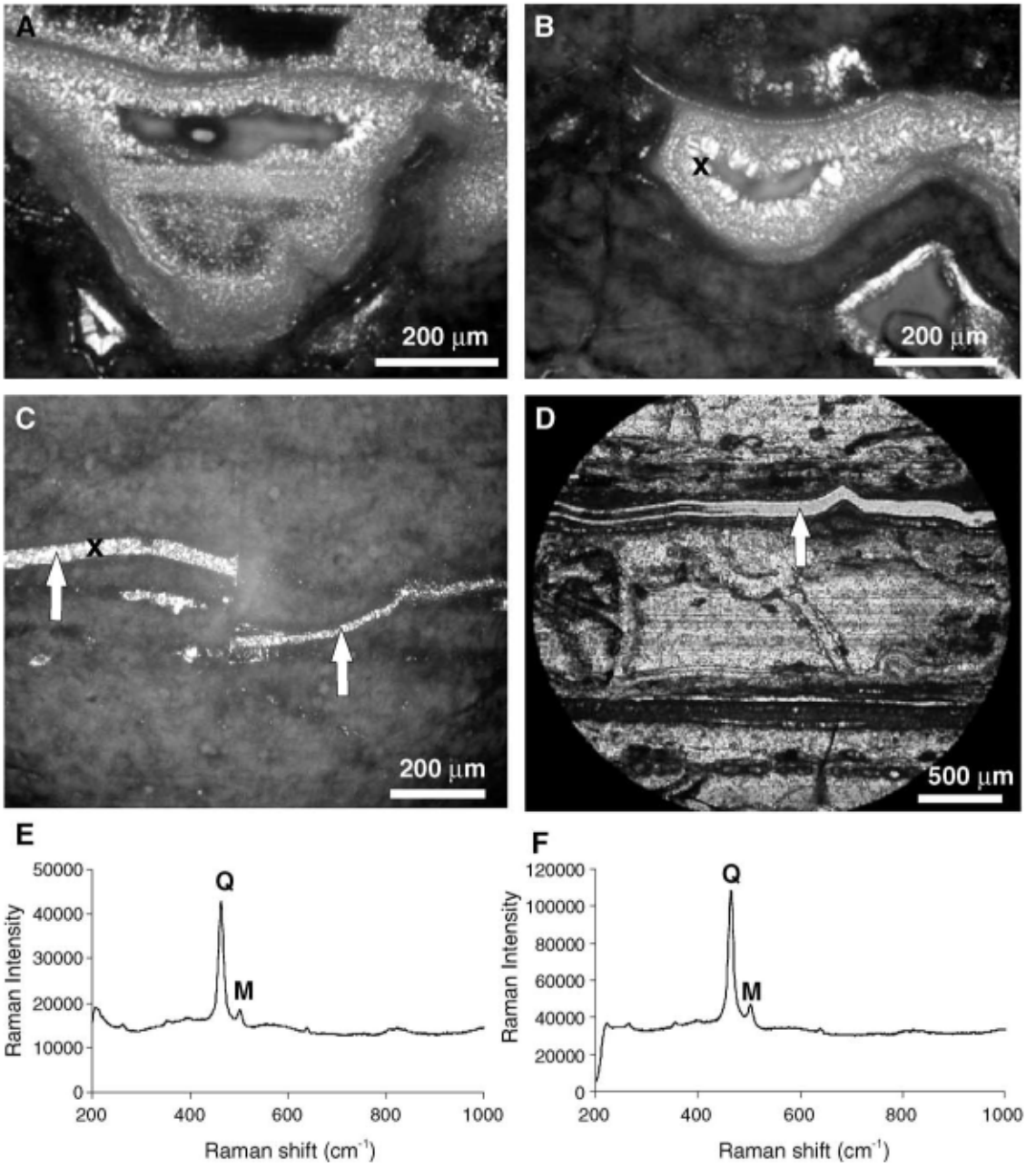

Fig. 13. Quartz in fractures and voids. (A–D) Thin section photomicrographs of sample AU55348 taken under cross-polarized light. (A) Geopetal infill of void with microcrystalline quartz. (B) Well-developed quartz crystals occur inside the void, with the largest crystals growing into the void space; x = location of Raman microprobe scan shown in (E). (C) Faulted, undulose band of microcrystalline quartz (bright) with sharp boundaries, in a groundmass of fine-grained (gray) opal-CT; x = Raman microprobe scan shown in F. (D) Microcrystalline quartz vein (arrow) in a groundmass of fine-grained opal-CT. (E–F) Raman microprobe scans. (E) Both quartz and moganite occur in the quartz crystals that grow into the void shown in (B). (F) Quartz and moganite in the microcrystalline quartz band shown in (C).

7. Discussion

7.1. Geothermal activity at opal mound

Two periods of discharge at Opal Mound have produced a ~1600-year-old sinter on distal slopes that is mineralogically immature and brightly colored, and a ~1900-year-old sinter in proximal vent areas that is mineralogically mature and white. Movement along the Opal Mound fault opened conduits, allowing fluids to discharge at the surface as well as fracturing older sinter. Injection of thermal fluids into fractures would have provided a medium to move silica, and conductively heat the sinter surrounding the fractures, possibly accelerating diagenesis. Opal Mound has not been exposed to post-depositional fumarolic overprinting, as there are few dissolution features, and none of the typical hydrothermal alteration minerals are present that would indicate steam condensate.

Distal-apron sinter deposits are chronologically the youngest deposits at the Opal Mound and mineralogically the least mature, even though they occur at the lowest elevations. Hence, sites of spring discharge likely migrated from higher to lower elevations, as has occurred at Orakei Korako, in the Taupo Volcanic Zone, New Zealand (cf. Lloyd, 1972). There, thermal fluids currently discharge on terraces at elevations ~30 m below the sites of extinct springs and older sinter deposits. Such changes may reflect a lowering of the water table and progressive sealing of the early, higher-elevation vents.

7.2. Sinter diagenesis – mineralogic changes

At incremental mineralogical stages — opal-A, opal-A/CT, opal-CT, opal-C and quartz — several morphologies co-exist such as aligned nanospheres+bladed lepispheres or nano-structures+microcrystals, confirming that silica transformations during diagenesis occur gradually and gradationally. Campbell et al. (2001) recognized patchy replacement textures in sinter where silica phase transformations at the micro-scale occur gradually and gradationally over lateral and stratigraphic distances of millimeters. Putnis (1992) reported that a change from one silica polymorph to another, such as from tridymite to cristobalite or quartz, requires bond breakage and creation of a new structure. This process causes reconstructive transformations and provides a mechanism for extremely fine-scale intergrowths between the different polymorphs, allowing co-existence of more than one silica phase at any given time.

At Opal Mound, there is an overall increase in density as diagenesis proceeds, a trend also recorded for sinters in New Zealand (Herdianita et al., 2000a). However, some mineralogically immature samples at Opal Mound have higher densities than opal-A samples from New Zealand. At Opal Mound, porosities are <15% regardless of the mineralogy. By contrast, Herdianita et al. (2000a) reported a porosity decrease with maturation in New Zealand sinters. The variability in densities and porosities between Opal Mound sinter and New Zealand sinters can be explained by differences in the original sinter fabric type. Immature sinter from Opal Mound is dominantly well indurated, whereas early diagenetic samples from New Zealand typically constitute porous friable sinter (cf. Lynne and Campbell, 2003, 2004). The latter also subsequently transforms to vitreous quartz with maturation. Therefore, the transformation of well-indurated opal-A to vitreous quartz at Opal Mound likely requires less marked density and porosity changes because the fabric changes during maturation are less dramatic.

7.3. Sinter diagenesis – morphological changes

Sinter diagenesis at Opal Mound begins with the transformation of smooth, opal-A microspheres, ~8 μm in diameter, into opal-A/CT nanospheres with diameters of ~200 nm. This particle size-change suggests dissolution of the microspheres and reprecipitation of the silica into smaller silica packages. According to Brown (1990), dissolution of the outer surfaces is followed by absorption of silica back into the newly formed structure. At Opal Mound, silica dissolved from the outer surfaces of rows of aligned nanospheres of opal-A/CT is reprecipitated as incipient opal-CT. This process fills spaces between remnant nanospheres and covers surfaces to produce the transitional, beaded, jagged-edged features and then classic, sharply bladed structures of paracrystalline opal-CT. At Opal Mound, the 1-μm-long rows of aligned nanospheres groups are the same length as the individual blades they become within each opal-CT lepisphere (cf. Fig. 7 to Fig. 8). Both aligned nanospheres and beaded blades show

multiple orientation directions. Hence, the transformation of aligned nanospheres to opal-CT bladed lepispheres involves dissolution and reprecipitation to a more advanced state (cf. Rodgers et al., 2004). Well-preserved, sharply bladed opal-CT lepispheres are well-known in sinter deposits (e.g., Campbell et al., 2001; Lynne and Campbell, 2003, 2004). However, recognition of the early alignment of nanospheres at the Opal Mound as their precursor is a new finding. Subsequently, the typical bladed opal-CT lepispheres morphologically restructure themselves into 200 nm-long, opal-C nano-rods, also a newly identified incremental step to opal-C. The opal-C nano-rods and blocky nanostructures are the building blocks for the developing quartz crystals, the mature end-point of sinter diagenesis.

Recognition of the morphological transitions of aligned nanospheres (early opal-CT formation; Fig. 7) and blocky nanostructures (opal-C and early quartz formation; Fig. 10) is important because particle size affects reactivity. In general, the rate of phase transformation of a particle is accelerated when particles are small because of the greater number of nucleation sites per unit volume, thus increasing the energy within the atoms (Banfield and Hamers, 1979). This energy is used to overcome activation barriers, which restrict reaction rates. Thus, reaction rates are likely accelerated at the stages in diagenesis where nano-sized particles (e.g., nanospheres and nano-rods) are found.

Crystal defects also affect the rate at which solids react (Reeder and Rakovan, 1999). Crystal defect locations are high energy sites where lower activation barriers exist, enhancing crystal growth (Jamtviet and Meakin, 1999). At Opal Mound bumpy nanospheres, aligned rows of opal-A/CT nanospheres, jagged blade-edges of incipient opal-CT lepispheres, and opal-C nano-rods and nanostructures all have uneven microtopography and therefore could be considered sites of high reactivity. Early diagenetic quartz crystals at Opal Mound also display stepped and uneven surfaces intercalated with bands of blocky opal-C nanostructures (Figs. 3 and 10E, F), prior to their modification into smooth, doubly terminated quartz crystals. Furthermore, morphological and mineralogical changes during diagenesis may proceed quickly through the stages where crystal defects are present. Hence, capturing the morphological development of these step-size mineralogical modifications is difficult because they are transitory and occur within a relatively narrow diagenetic window (cf. Fig. 3). Sinter must be "frozen" in time and sampled at particular intervals in the diagenetic gradient in order to record these ephemeral but critical phases in the maturation from opal-A to quartz.

8. Conclusions

Sinter deposited at Opal Mound is unusual because it displays the complete sequence of diagenetic changes from opal-A to quartz which occurred within 1900 years, a shorter time than other known old sinter deposits (cf. Herdianita et al., 2000a). Systematic differences in morphology and mineralogy occur from vent and proximal-vent sinters, through to mid- and distal-slope deposits. Each of the five recurring mineralogical steps in the progressive diagenesis of the sinter deposit (opal-A, opal-A/CT, opal-CT, opal-C, and quartz) also are typified by specific morphologies, and shifts in particle sizes of the ensuing nano- and microtextures. Transitional morphological states, represented by opal-A/CT nanospheres and opal-C nano-rods, are not commonly preserved because they consist of nanometer-sized particles that are susceptible to rapid change to a more mature silica phase, probably via dissolution and reprecipitation. The diagenetic alteration of opal-A to early opal-CT is marked by the formation of 1-μm-long rows of 200-nm-diameter nanospheres, which become aligned before they convert into same-sized blades of classic opal-CT lepispheres. The transition from opal-CT to opal-C occurs when lepispheres of opal-CT reorganize to form 200-nm-long nano-rods. Incipient quartz is visible where quartz and opal-C occur as 200-nm-sized clusters of blocky nanostructures. Moganite co-exists in abundance with opal-CT and, in lesser amounts, with opal-C and diagenetic quartz. By contrast, late-stage, fibrous, hydrothermal quartz lacks any moganite. At all stages during sinter maturation, mineralogical changes precede morphological changes, and transitions between the silica phases are both gradual and gradational. A shift to larger d-spacings in XRPD peak position is the first indication of an imminent silica phase change.

The transformation from opal-A to quartz in the white vitreous, northern vent and near-vent samples at Opal Mound has occurred within 1900 years. By contrast, colorful distal-slope sinter (1600 years BP) has remained relatively immature mineralogically, with only opal-A and opal-A/CT present. Trace element content fluctuated spatially and temporally, and was fluid controlled. Microbial communities appear to have had no influence on trace element distribution in the Roosevelt sinter. Conductive heat and the addition of silica from the injection of post-depositional, silica-rich fluids into the near-vent sinter may have accelerated diagenesis and formed secondary quartz veins in this part of the deposit.

This detailed macro-micro- and nano-scale study using multiple techniques places the Opal Mound sinter in a spatial and temporal context that delineates a paragenetic sequence with two main phases of thermal fluid influx. Furthermore, this study illustrates the complexity of paleoenvironmental and diagenetic conditions that can be extracted from sinter deposits preserved in the stratigraphic record.

Diagenetic transformations at Opal Mound confirm that the generalized paragenetic sequence recognized in New Zealand sinters (Campbell et al., 2001; Rodgers et al., 2004) can be broadly applied to hot spring deposits elsewhere. Some patterns recur in sinters from both Opal Mound, Utah, and the TVZ, New Zealand, implying similar developmental and diagenetic pathways. Regardless of the environmental conditions, or the microscale physico-chemical changes, the start and finish of the diagenetic process is always the same — given enough time (also variable), an opaline deposit transforms into a quartzose deposit. Depositional and post-depositional conditions should also be considered when determining a paragenetic sequence. For example, the Opal Mound sinter deposit contains fibrous microcrystalline quartz, formed after the sinter deposited. At Yellowstone, Guidry and Chafetz (2003b) reported both length-fast and length-slow chalcedony forming contemporaneously with opal-A where it formed in the throat of a vent, evidentially as an early deposited precipitate. Thus, we seek to observe the mineralogic and morphologic pathways of this transition, at all spatial and temporal scales, in order to identify recurring themes and processes in siliceous mineral diagenesis in geothermal environments.

Acknowledgment

This research was funded by the Foundation for Research Science and Technology through a Top Achievers Doctoral scholarship, and the New Zealand Federation of Graduate Women. The Geology Department and Research Centre for Surface and Materials Science (University of Auckland), and the Energy and Geoscience Institute (University of Utah) and Australian National University, provided technical support and equipment. In particular we thank David Langton, Catherine Hobbis, Louise Cotterall, John Wilmshurst, Ritchie Sims, Pablo Leterlier, Andrés Arcila, Bryony James and Katie Dowell. Two anonymous reviewers gave helpful suggestions that improved the paper.

References

Armstrong, R.L., 1970. Geoochronology of tertiary igneous rocks, eastern basin and range province, western Utah, eastern Nevada, and vicinity, U.S.A. Geochimica et Cosmochimica Acta 34, 203–232.

Bamford, R.W., Christensen, O.D., Capuano, R.M., 1980. Multi-Element Geochemistry of Solid Material in Geothermal Systems and Its Application. Part 1: the Hot Water System at the Roosevelt Hot Springs KGRA, Utah, Earth Science Laboratory Report, vol. 30. University of Utah Research Institute, pp. 1–168.

Banfield, J.F., Hamers, R.J., 1979. Processes of minerals and surfaces with relevance to microorganisms and prebiotic synthesis. In: Banfield, J., Nealson, K. (Eds.), Reviews in Mineralogy 35. Geomicrobiology: Interactions Between Microbes and Minerals, pp. 81–122.

Battey, M.H., Pring, A., 1977. Mineralogy for Students. Longman, Edinburgh.

Blackett, R.E., Ross, H.P., 1992. Recent exploration and development of geothermal resources in the Escalante Desert region, southwestern Utah. In: Harty, K.M. (Ed.), Engineering and Environmental Geology of Southwestern Utah. Utah Geological Association Publication 21. 1992 Field Symposium, pp. 261–280.

Brown Jr., G.E., 1990. Spectropscopic studies of chemisorption reaction mechanisms at oxide–water interfaces. In: Hochella Jr., M.F., White, A.F. (Eds.), Reviews in Mineralogy 23. Mineral–Water Interface Geochemistry, pp. 309–363.

Cady, S.L., Farmer, J.D., 1996. Fossilization processes in siliceous thermal springs: trends in preservation along thermal gradients. In: Bock, G.R., Goode, J.A. (Eds.), Evolution of Hydrothermal Ecosystems on Earth (and Mars?). Proceedings of the CIBA Foundation Symposium 202. Wiley, Chichester, U.K., pp. 150–173.

Campbell, K.A., Sannazzaro, K., Rodgers, K.A., Herdianita, N.R., Browne, P.R.L., 2001. Sedimentary facies and miner-

alogy of the Late Pleistocene Umukuri silica sinter, Taupo Volcanic Zone, New Zealand. Journal of Sedimentary Research 71, 727–746.

Campbell, K.A., Buddle, T.F., Browne, P.R.L., 2004. Late Pleistocene silica sinter associated with fluvial, lacustrine, volcaniclastic and landslide deposits at Tahunaatara, Taupo volcanic zone, New Zealand Transactions of the Royal Society of Edinburgh. Earth Sciences 94, 485–501.

Capuano, R.M., Cole, D.R., 1982. Fluid–mineral equilibria in high temperature geothermal systems. The Roosevelt Hot Springs geothermal system, Utah. Geochimica et Cosmochimica Acta 46, 1353–1364.

Cassie, V., 1989. A taxonomic guide to thermally associated algae (excluding diatoms) in New Zealand. Bibliotheca Phycologica 78, 1–159.

Christensen, O.D., Capuano, R.M., Moore, J.N., 1983. Trace element distribution in an active hydrothermal system, Roosevelt Hot Springs thermal area, Utah. Journal of Volcanology and Geothermal Research 16, 99–129.

Eggins, S.M., Woodhead, J.D., Kinsley, L.P.J., Sylvester, P., McCulloch, M.T., Hergt, J.M., Handler, M.R., 1997. A simple method for the precise determination of greater-than-or-equal-to 40 trace elements in geological samples by ICP-MS using enriched isotope internal standardization. Chemical Geology 134, 311–326.

Farmer, J.D., 1999. Taphonomic modes in microbial fossilization. Size Limits of Very Small Micro-organisms. Proceedings of a Workshop, Space Studies Board, Commission on Physical Sciences, Mathematics Applications, National Research Council. National Academy Press, Washington, D.C., pp. 94–102.

Flörke, O.W., Graetsch, H., Martin, K., Roller, K., Wirth, R., 1991. Nomenclature of micro- and non-crystalline silica minerals, based on structure and microstructure. Neues Jahrbuch für Mineralogie Abhandlungen 163, 19–42.

Fournier, R.O., Rowe, J.J., 1966. Estimation of underground temperatures from the silica content of water from hot springs and steam wells. American Journal of Science 264, 685–697.

Götze, J., Nasdala, L., Kleeberg, R., Wenzel, M., 1998. Occurrence and distribution of "moganite" in agate/chalcedony: a combined micro-Raman, Rietveld and cathodoluminescence study. Contributions to Mineralogy and Petrology 133, 96–115.

Graetsch, H., 1994. Structural characteristics of opaline and microcrystalline silica minerals. In: Heaney, P.J., Prewitt, C.T., Gibbs, G.V. (Eds.), Silica: Physical Behaviour, Geochemistry and Materials Applications, Reviews in Mineralogy, vol. 29. Mineralogical Society of America, Washington, D.C., pp. 209–232.

Grotzinger, J.P., Knoll, A.H., 1999. Stromatolites in Precambrian carbonates: evolutionary mileposts or environmental dipsticks? Annual Review of Earth and Planetary Sciences 27, 313–358.

Guidry, S.A., Chafetz, H.S., 2003a. Depositional facies and diagenetic alteration in a relict siliceous hot spring accumulation: examples from Yellowstone National Park, U.S.A. Journal of Sedimentary Research 73, 806–823.

Guidry, S.A., Chafetz, H.S., 2003b. Anatomy of siliceous hot springs: examples from Yellowstone National Park, Wyoming, USA. Sedimentary Geology 157, 71–106.

Guidry, S.A., Chafetz, H.S., 2003c. Siliceous shrubs in hot springs from Yellowstone National Park, Wyoming, U.S.A. Canadian Journal of Earth Sciences 40, 1571–1583.

Herdianita, N.R., Browne, P.R.L., Rodgers, K.A., Campbell, K.A., 2000a. Mineralogical and textural changes accompanying ageing of silica sinter. Mineralium Deposita 35, 48–62.

Herdianita, N.R., Rodgers, K.A., Browne, P.R.L., 2000b. Routine instrumental procedures to characterise the mineralogy of modern and ancient silica sinters. Geothermics 29, 65–81.

Jamtviet, B., Meakin, P., 1999. Growth, dissolution and pattern formation in geosystems. In: Jamtveit, B., Meakin, P. (Eds.), Growth, Dissolution and Pattern Formation in Geosystems. Kluwer Academic Publishers, London, pp. 143–162.

Jones, B., Segnit, E.R., 1971. The nature of opal[2]: nomenclature and constituent phases. Journal of the Geological Society of Australia 18, 57–68.

Jones, B., Renaut, R.W., Rosen, M.R., 1997. Vertical zonation of biota in microstromatolites associated with hot springs, North Island, New Zealand. Palaios 12, 220–236.

Jones, B., Renaut, R.W., Rosen, M.R., 2001. Biogenicity of gold- and silver-bearing siliceous sinters forming in hot (>75 °C) anaerobic spring-waters of Champagne Pool, Waiotapu, North Island, New Zealand. Journal of the Geological Society (London) 158, 895–911.

Jones, B., Renaut, R.W., Rosen, M.R., 2004. Taxonomic fidelity of silicified filamentous microbes from hot-spring systems in the Taupo Volcanic Zone, North Island, New Zealand. Transactions of the Royal Society of Edinburgh. Earth Sciences 94, 475–483.

Kerr, R.A., 2000. Reversals reveal pitfalls in spotting ancient and E.T. life. Science 286, 1384–1385.

Kingma, K.J., Hemley, R.J., 1994. Raman spectroscopic study of microcrystalline silica. American Mineralogist 79, 269–273.

Knoll, A.H., Walter, M.R., 1996. The limits of palaeontological knowledge: finding the gold among the dross. In: Bock, G.R., Goode, J.A. (Eds.), Evolution of Hydrothermal Ecosystems on Earth (and Mars?), Ciba Foundation Symposium, vol. 202. John Wiley and Sons, Chichester, pp. 198–213.

Lloyd, E.F., 1972. Geology and hot springs of Orakei Korako. New Zealand Geological Survey Bulletin 85, 1–164.

Lowe, D.R., Anderson, K.S., Braunstein, D., 2001. The zonation and structuring of siliceous sinter around hot springs, Yellowstone National Park, and the role of thermophilic bacteria in its deposition. In: Reysenbach, A.-L., Voytek, M., Mancinelli, R. (Eds.), Thermophiles: Biodiversity, Ecology and Evolution. Kluwer Academic/Plenum Publishers, New York, pp. 143–166.

Lynne, B.Y., Campbell, K.A., 2003. Diagenetic transformations (opal-A to quartz) of low- and mid-temperature microbial textures in siliceous hot-spring deposits, Taupo Volcanic Zone, New Zealand. Canadian Journal of Earth Sciences 40, 1679–1696.

Lynne, B.Y., Campbell, K.A., 2004. Morphologic and mineralogic transitions from opal-A to opal-CT in low-temperature siliceous sinter diagenesis, Taupo Volcanic Zone, New Zealand. Journal of Sedimentary Research 74, 561–579.

Lynne, B.Y., Moore, J., Browne, P.R.L., Campbell, K.A., 2003. Age and mineralogy of the Steamboat Springs silica sinter deposit, Nevada, U.S.A.: a preliminary report of core SNLG 87-29. Proceedings 25th NZ Geothermal Workshop, pp. 65–70.

McKenzie, E.J., Brown, K.L., Cady, S.L., Campbell, K.A., 2001. Trace metal chemistry and silicification of microorganisms in geothermal sinter, Taupo Volcanic Zone, New Zealand. Geothermics 30, 483–502.

Merz, M.U.E., 1992. The biology of carbonate precipitation by cyanobacteria. Facies 26, 81–102.

Moore, J.M., Nielson, D.L., 1994. An overview of the geology and geochemistry of the Roosevelt Hot Springs geothermal system, Utah. Utah Geological Association Publication 23, 25–36.

Munsell Soil Colour Charts, 1992 revised edition. Munsell Colour, division of Kollmorgen Instruments Corporation.

Neilson, D.L., Sibbet, B.S., McKinney, D.B., Hulen, J.B., Moore, J.N., Samberg, S.M., 1978. Geology of Roosevelt Hot Springs KGRA, Beaver Country, Utah, Earth Science Laboratory Report, vol. 12. University of Utah Research Institute, pp. 1–120.

Park, G.M., 1971. Volcanics, Thomas Range. In: Whelean, J.A. (Ed.), Radioactive and Isotopic Age Determinations of Utah Rocks, Utah Geology and Mineral Survey Bulletin, vol. 81, pp. 1–23.

Parker, R.J., Nicholson, K., 1990. Arsenic in geothermal sinters: determination and implications for mineral exploration. Proceedings 12th NZ Geothermal Workshop, pp. 35–39.

Parry, W.T., Ballantyne, J.M., Bryant, N.L., Dedolph, R.E., 1979. Geochemistry of hydrothermal alteration at Roosevelt Hot Springs thermal area, Utah. Geochimica et Cosmochimica Acta 44, 95–102.

Putnis, A., 1992. Introduction to Mineral Sciences. Press Syndicate of the University of Cambridge, U.S.A.

Reeder, R.J., Rakovan, J., 1999. Surface structural controls on trace element incorporation during crystal growth. In: Jamtviet, B., Meakin, P. (Eds.), Growth, Dissolution and Pattern Formation in Geosystems. Kluwer Academic Publishers, London, pp. 143–162.

Ridley, W.I., Lichte, F.E., 1998. Major, trace and ultra trace element analysis by laser ablation ICP-MS. In: McKibben, M.A., Shanks III, W.C., Ridley, W.I. (Eds.), Applications of Microanalytical Techniques to Understanding Mineralisation Processes, Reviews in Economic Geology, vol. 7, pp. 199–215.

Rodgers, K.A., Cressey, G., 2001. The occurrence, detection and significance of moganite (SiO_2) among some silica sinters. Mineralogical Magazine 65, 157–167.

Rodgers, K.A., Hampton, W.A., 2003. Laser Raman identification of silica phases comprising microtextural components of sinters. Mineralogical Magazine 67, 1–13.

Rodgers, K.A., Browne, P.R.L., Buddle, T.F., Cook, K.L., Greatrex, R.A., Hampton, W.A., Herdianita, N.R., Holland, G.R., Lynne, B.Y., Martin, R., Newton, Z., Pastars, D., Sannazarro, K.L., Teece, C.I.A., 2004. Silica phases in sinters and residues from geothermal fields of New Zealand. Earth Science Reviews 66, 1–61.

Sibbett, B.S., Nielson, D.L., 1980. Geology of the central Mineral Mountains, Beaver Company, Utah, Earth Science Laboratory Report, vol. 33. University of Utah Research Institute, pp. 1–42.

Smith, D.K., 1997. Evaluation of the detectability and quantification of respirable crystalline silica by X-ray powder diffraction. Powder Diffraction 12, 200–227.

Smith, D.K., 1998. Opal, cristobalite, and tridymite: noncrystallinity versus crystallinity, nomenclature of the silica minerals and bibliography. Powder Diffraction 13, 2–19.

Smith, B.Y., Turner, S.J., Rodgers, K.A., 2003. Opal-A and associated microbes from Wairakei, New Zealand: the first 300 days. Mineralogical Magazine 67, 563–579.

Walter, M.R., Des Marais, D., Farmer, J.D., Hinman, N.W., 1996. Lithofacies and biofacies of mid-Paleozoic thermal spring deposits in the Drummond basin, Queensland, Australia. Palaios 11, 497–518.

Ward, S.H., Parry, W.T., Nash, W.P., Sill, W.R., Cook, K.L., Smith, R.B., Chapman, D.S., Brown, F.H., Whelan, J.A., Bowman, J.R., 1978. A summary of the geology, geochemistry and geophysics of the Roosevelt Hot Springs thermal area, Utah. Geophysics 43, 1515–1542.

White, D.E., Thompson, G.A., Sandberg, C.H., 1964. Rocks, structure, and geologic history of Steamboat Springs thermal area, Washoe County, Nevada. Geological Survey Professional Paper 458-B, 1–63.